JOURNAL OF GEOMAGNETISM AND GEOELECTRICITY

VOL. IX NO. 2

SOCIETY
OF
TERRESTRIAL MAGNETISM AND ELECTRICITY
OF
JAPAN

1957
KYOTO

JOURNAL OF GEOMAGNETISM AND GEOELECTRICITY

EDITORIAL OFFICE: Society of Terrestrial Magnetism and Electricity of Japan, Geophysical Institute, Kyoto University, Kyoto, Japan

The fields of interest of this quarterly Journal are as follows:

Terrestrial Magnetism	Aurora and Night Airglow
Atmospheric Electricity	The Ozone Layer
The Ionosphere	Physical States of the Upper Atmosphere
Radio Wave Propagation	Solar Phenomena relating to the Above Subjects
Cosmic Rays	Electricity within the Earth

The text should be written in English, German or French. The price is set as 1 dollar per number. We hope to exchange this Journal with periodical publications of any kind in the field of natural science.

The Editors

Thermo-Remanent Magnetism and Coercive Force of the Ilmenite-Hematite Series.*

By Seiya UYEDA

Geophysical Institute, Tokyo University
Earthquake Research Institute, Tokyo University

(Read on May 12, 1957; Received on July 10, 1957)

Abstract

The thermo-remanent magnetism and the coercive force of the ilmenite-hematite solid solution $(1\text{-}x)\,Fe_2O_3 \cdot x FeTiO_3$ have been examined for the range $0<x<0.7$: in the range $x>0.7$, the solid solution is only paramagnetic at room temperature. The specimens are all synthesized ones. Measured quantities are $J(T)$, $J_r(T)$, $H_c(T)$ and $H_{cr}(T)$ for the maximum field of 800 *Oe.* and the TRM $[J_{T_c,\ H=2.0\ oe.}^{T_0}(T)]$. The summarized results are as follows: In the parasitically ferromagnetic region ($x<0.5$), $J(T)$ and $J_r(T)$ show an increase below the Curie point, while $H_c(T)$, and $H_{cr}(T)$ decrease monotonously with temperature. Thermo-remanent magnetism is strong in comparison with $J(T)$ in this region, the Q-ratio amounting to several hundred. In the ferrimagnetic region ($0.7>x>0.5$), $J(T)$ and $J_r(T)$ show the typical straight decrease with temperature rise. H_c and the Q-ratio are quite smaller than for the parasitically ferromagnetic region. Remarkable reverse TRM like the Haruna-type one appears for the specimens of the range bordering the ferrimagnetic and parasitically ferromagnetic regions, namely the range $0.6>x>0.45$. This indicates that the phenomenon is inherent to this substance and is closely related to the fundamental magnetic properties of this series. Furthermore, it was found that a definite tendency for reverse TRM appears for $x \fallingdotseq 0.1$ that may be relevant to the natural reverse remanence of Adirondack rocks reported by Balsley and Buddington. Stability against the AC demagnetization and the field dependence of the thermo-remanent magnetism of this series have also been examined systematically.

1. Introduction

Ferromagnetism or ferrimagnetism of certain members of the system ilmenite-hematite has recently been discovered in the course of the study on the mechanism of the reverse thermo-remanent magnetism (reverse TRM) [1]. Since then, a thorough examination of magnetic properties of this system has been conducted to establish the following facts [2]: when the chemical composition of a member of this system is expressed by $(1-x)\,Fe_2O_3 \cdot x FeTiO_3$, the members in the region $0<x<0.5$ are antiferromagnetics with weak parasitic ferromagnetism and those in the region $0.5<x<0.7$

* Contribution from Division of Geomagnetism and Geoelectricity, Geophysical Institute, Tokyo University. Series II, No. 69

are ferrimagnetics at the room temperature. The members with $x>0.7$ are also ferrimagnetics but their Curie point is below the room temperature, whereas the members with $x \fallingdotseq 1$ are reported as antiferromagnetics with very low Néel point [3]. The complicated magnetic characteristics of this series are explained in detail in terms of an order-disorder transformation of *Fe* and *Ti* ions in the crystal structure by Y. Ishikawa and S. Akimoto [4].

Although the natural occurrence of this series in nature is rarer than that of the titano-magnetite series, its importance in rock-magnetism is great because of the various peculier characteristics revealed in its thermo-remanent and natural remanent magnetism. For instance, it is precisely members of this series that shows the reverse TRM of the Haruna-type [5], [6]. In a previous paper, the author showed that many of natural samples belonging to the ferrimagnetic region of this series can acquire the capability of producing the reverse TRM by simple heat treatment [7]. Moreover, the natural reverse remanent magnetism of the pre-Cambrian rocks of the Adirondack Mountains, U.S.A., was suggested to be caused by some yet unknown self-reversal mechanism inherent to this series [8]. The pronounced negative geomagnetic anomaly at Allard Lake, Ontario, Canada was also suggested to be due to the reverse natural magnetization of the vast ilmenite-hematite deposit at that area [9]. The abnormal characteristics of this series with respect to remanent magnetism is so marked that it has been proposed that any rock containing this series should be excluded from the object of the palaeomagnetic studies [10].

On the other hand, the natural remanent magnetism of pure hematite has been proved to be useful for palaeomagnetic studies because of its extremely high stability. Its thermo-remanent properties has already been studied fairly in detail [11].

Considering these facts, it may be noticed that such a systematic examination of thermo-remanent properties of this series as has been done for rocks containing titano-magnetites by T. Nagata [12] is necessary for further development of rock-magnetism. In the present study, the author has conducted a study to clarify the normal and abnormal characteristics of the TRM of this series by using synthesized solid solutions with varying ratio of ilmenite to hematite. The thermal variation of the coercive force, which may have important bearings to the TRM [13], has also been measured.

2. The Specimens

In order to examine the characteristics of TRM of the ilmenite-hematite series systematically, we prepared series of solid solutions $(1-x)\,Fe_2O_3 \cdot x FeTiO_3$ with x at every 0.1 approximately, from $x \fallingdotseq 0$ to $x \fallingdotseq 0.7$. The solid solutions in the ilmenite side range ($x>0.7$) were not used in the present study because they are only paramagnetic at room temperature (T_0). The method for synthesis was similar to that described by T. Nagata and S. Akimoto [2]; a mixture of fine powders of ilmenite and hematite in a given ratio is enclosed in a quartz tube evacuated, at room temperature, to as low as 10^{-3} mmHg in air pressure, and quenched after being kept at 1200°*C* for 8 hours. For ilmenite, we used the carefully purified ferromagnetic ilmenite of Himesima iron

Table I. Characteristics of the synthesized normal ilmenite-hemotite solid solution series.
x-value in the expression $(1-x)\,Fe_2O_3 \cdot x\,FeTiO_3$ *is listed in the first column: this is used to specify the specimen throughout the text.*

chemical composition					lattice parameters		T_c°C	$J(T_0)$ emu/cc	$J_r(T_0)$ emu/cc	$H_c(T_0)$ oersteds	$H_{cr}(T_0)$ oersteds	TRM $J_{T_c}^{T_0}$ 2.0 Oe. (T_0) emu/cc	Q−ratio for 2.0 Oe
x-value	total wt. % of $FeO+Fe_2O_3+TiO_2$	FeO*	Fe_2O_3*	TiO_2*	a_{rh}	α_{rh}							
0.01	99.68	1.19	98.81	—	5.426 Å	55°16′	670	19.3×10^{-2}	9.7×10^{-2}	360	560	34.0×10^{-2}	705
0.09	95.13	6.61	84.15	9.24	5.428	55 17	595	13.0×10^{-2}	8.2×10^{-2}	400	525	10.9×10^{-2}	336
0.17	91.22	13.25	70.79	15.96	5.440	55 13	525	8.6×10^{-2}	5.1×10^{-2}	400	600	16.6×10^{-2}	770
0.28	96.60	19.93	56.85	23.22	5.451	55 10	440	17.4×10^{-2}	11.4×10^{-2}	350	520	27.5×10^{-2}	630
0.41	99.29	28.20	42.00	29.80	5.461	55 08	350	27.2×10^{-2}	16.4×10^{-2}	275	325	24.4×10^{-2}	365
0.48	79.55	29.85	35.02	35.13	5.471	55 06	260	34.5×10^{-2}	11.3×10^{-2}	215	375	15.4×10^{-2}	179
0.60	96.56	35.59	24.71	39.69	5.478	55 03	200	21.7	2.8	117	580	−1.94	−36
0.71	93.85	39.45	17.10	43.45	5.489	54 59	70	44.8	14.7	85	136	16.0	5

* in mol %
J, J_r, H_c and H_{cr} are for $H=800$ *Oe*.

Table II Characteristics of the synthesized abnormal ilmenite-hematite solid solution series.

chemical composition					lattice parameters		T_c°C	$J(T_0)$ emu/cc	$J_r(T_0)$ emu/cc	$H_c(T_0)$ oersteds	$H_{cr}(T_0)$ oersteds	TRM $J_{T_c}^{T_0}$ 2.0 Oe. (T_0) emu/cc	Q-ratio for 2.0 Oe.
x-value	total wt. % of $FeO+Fe_2O_3+TiO_2$	FeO*	Fe_2O_3*	TiO_2*	a_{rh}	α_{rh}							
0.02	85,05	4.61	95.40	—	5.398 Å	55°20′	570	16.6×10^{-2}	5.8×10^{-2}	210	300	26.0×10^{-2}	622
0.13	79.60	10.10	77.25	12.66	5.413	55 17	540	14.4×10^{-2}	8.7×10^{-2}	425	600	11.4×10^{-2}	336
0.23	88.71	18.04	61.53	20.43	5.423	55 15	460	13.7×10^{-2}	8.5×10^{-2}	200	250	21.0×10^{-2}	600
0.32	88.31	22.31	51.83	25.86	5.437	55 13	410	15.8×10^{-2}	6.0×10^{-2}	82	140	21.0×10^{-2}	500
0.42	92.94	27.48	40.52	32.00	5.451	55 09	330	16.6×10^{-2}	7.9×10^{-2}	80	200	11.4×10^{-2}	355
0.45	95.13	29.52	37.76	32.72	5.455	55 09	300	14.1×10^{-2}	5.8×10^{-2}	115	380	7.9×10^{-2}	225
0.51	90.32	31.87	32.74	35.39	5.464	55 05	270	49.5×10^{-2}	8.4×10^{-2}	130	320	8.4×10^{-2}	70
0.56	95.00	34.51	28.50	36.99	5.468	55 06	220	3.14	5.2×10^{-1}	150	675	−35.8	−26

* in mol %
J, J_r, H_c and H_{cr} are for $H=800$ *Oe*.

sand, of which chemical composition had previously been determined [7]. For hematite we used two kinds of artificial hematite of different origins: one was synthesized by heating of ferric hydroxide which was precipitated by ammonium hydroxide from ferric chloride solution, and the other was a commercial guaranteed reagent, both having been ascertained to be chemically and crystallographically pure hematite.

In the following, the series made from the former hematite will be called the ***normal series,*** and the one from the latter the ***abnormal series*** by the reason described below.

The lattice parameters of all the specimens were obtained by a "Norelco" diffractometer as listed in Tables I and II. The spectrograms of all these specimens show exclusively the spectra of rhombohedral crystal structure. Within the limit of the resolving power of the "Norelco," all specimens were found to be crystallographically homogeneous. Trace of neither the cubic titanomagnetite series nor the orthorhombic pseudobrookite series could be found [2].

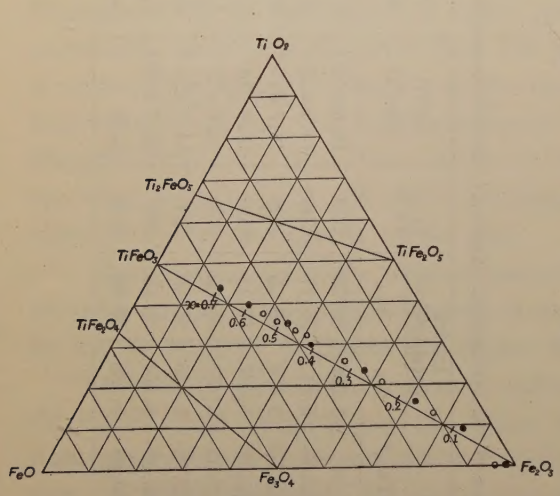

Fig. 1 Chemical composition of synthesized ilmenite-hematite series, represented on a FeO-TiO_2-Fe_2O_3 ternary diagram.
• ....*normal series*, ○ ....*abnormal series*.

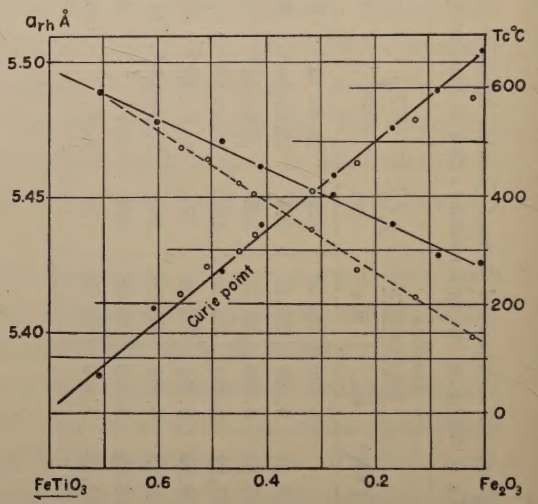

Fig. 2 Rhombohedral lattice parameter a_{rh} and Curie point T_c of syntheisized ilmenite-hematite series as dependent on chemical composition.
• ....*normal series*, ○ ....*abnormal series*.

The chemical composition obtained by chemical analysis after synthesis of the specimens is also shown in Tables I and II and in Fig. 1. Fig. 2. shows the relations between the lattice parameter a_{rh} and the Curie point T_c obtained by the thermomagnetic analysis and the chemical composition of the specimens. In Figs. 1 and 2, the full circles and the hollow ones are for the *normal* and *abnormal* series respectively. In Fig. 2, it is rather remarkable that, although the lattice parameter a_{rh} and the Curie point T_c of the specimens of the *normal series* are in good agreement with what has been determined for the ilmenite-hematite series by T. Nagata and S. Akimoto [2], a_{rh} and T_c of the *abnormal series* considerably deviate from them. Since the values of a_{rh} and T_c of the *normal series* agree with the generally accepted ones, we regard the specimens of the *normal series* as having the normal characteristics of ilmenite-hematite

solid solution and those of the *abnormal series* as somewhat abnormal. Though the observed difference in a_{rh} of the two series must have been caused by some subtle difference in the nature of the two kinds of hematite mentioned above, it has been not possible to clarify the reason any more. The grain size of the specimens used in the present study was always kept at about 10μ in mean diameter, so that the differences in magnetic properties due to the grain size effect may be regarded as eliminated.

3. The Method of Measurement

The magnetic measurements in the present study have been conducted by a ballistic method. The apparatus used is similar to the one reported by us previously [14], the major difference from the latter being that the present one is equipped with a solenoid coil that can produce a magnetic field as intense as 800 *Oe.*

In the first place, the measurements of the thermal variations of magnetization $J(T)$, of remanent magnetization $J_r(T)$, of coercive force $H_c(T)$, and of remanent coercive force $H_{cr}(T)$, during heating have been made on each specimen. These measurement were carried out by drawing hysteresis loops at successively higher temperatures. Definitions of these quantities are as usual and shown in Fig. 3. The remanent coercive force, $H_{cr}(T)$, is a coercive force of remanent magnetization measured at null magnetic field. In the cooling process, the mode of development of the total thermo-remanent magnetism has been measured in a magnetic field of 2.0 *Oe.* on each specimen.

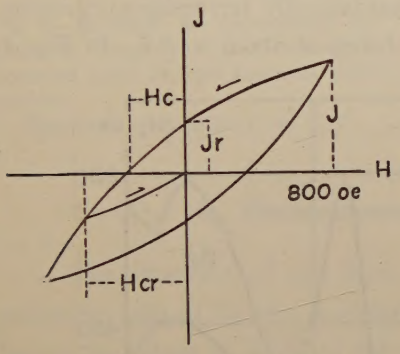

Fig. 3 Schematic representation of the magnetization curve.

For the measurement of the thermal variation of coercive force of rocks and ferromagnetic minerals; there have recently been reported two methods, one by a cathode-ray oscilloscope using alternating magnetic field [15], and the other by a magnetic balance [16]. In order to measure other quantities simultaneously as in the present study, such a classical ballistic method as employed here is most useful.

The limitation in the present apparatus is that the intensity of the magnetic field available by the solenoid coil can not exceed 800 *Oe.*, so that the measured values of $J(T)$, $J_r(T)$, $H_c(T)$ and $H_{cr}(T)$ differ from those measured using a magnetic field sufficiently intense to saturate the specimen. The results of these experiments will be described in §§ 4–7.

After the series of measurements mentioned above, the stability of the thermo-remanent magnetism was examined for each specimen, by means of demagnetization by alternating magnetic field. The results are reported in § 8.

Finally, the dependence of the thermo-remanent magnetism on the intensity of the magnetic field applied during cooling was studied for each specimen (§ 9). For some specimens, the characteristics of the partial thermo-remanent magnetism which

is produced by applying a magnetic field only within some restricted temperature range during cooling and of the addition law of thermo-remanent magnetism [12] were also examined (§ 7).

In magnetic measurements of the ilmenite-hematite series, the existence of magnetite impurity must be carefully avoided. Since the magnetism of the titano-magnetite series is much stronger than that of the parasitic ferromagnetism of the ilmenite-hematite series, it sometimes is necessary for accurate measurement to reduce the amount of the impurity less than 1/100,000 in weight, which is certainly undetected by *X*-ray techniques. Selective dissolution of the titano-magnetite series by hydrochloric acid has been utilized for the elimination of it.

4. Intensities of Magnetization and Remanent Magnetization at Room Temperature. [$J(T_0)$ and $J_r(T_0)$.]

The intensity of magnetization at room temperature $J(T_0)$ changes with the ilmenite-content (x) but not linearly. The value of $J_r(T_0)$ varies in the same way as $J(T_0)$, as observed in Fig. 4, in which circles and triangles represent the values of $J(T_0)$ and $J_r(T_0)$ for a magnetic field of 800 *Oe*. The range between ilmenite-hematite is, as already mentioned, divided into two parts, namely the parasitically ferromagnetic region and the ferrimagnetic region, the border of the two being at about $x=0.5$. In Fig. 4

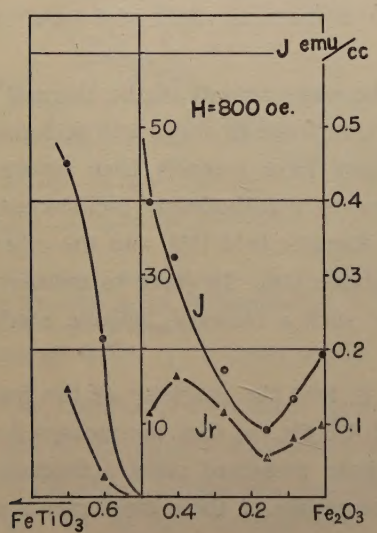

Fig. 4 Intensity of magnetization J and of remanent magnetization J_r, at room temperature, of the *normal series* of ilmenite-hematite solid solution as dependent on chemical composition; magnetic field applied is 800 *Oe*.

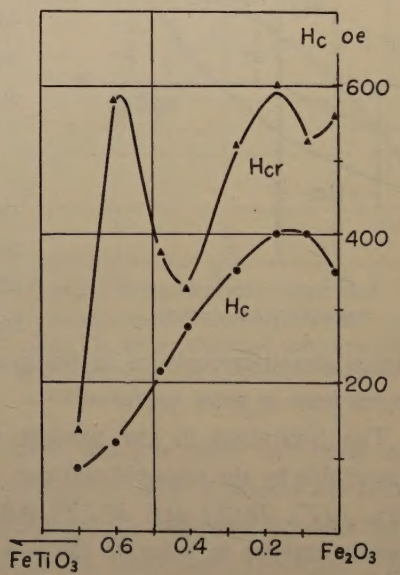

Fig. 5 Coercive force H_c and remanent coercive force H_{cr}, at room temperature, of the *normal series* of ilmenite-hematite solid solution as dependent on chemical composition; maximum magnetic field applied is 800 *Oe*.

the scale of the ordinate for the region $x>0.5$ is 10^2 times that of the region $x<0.5$. These values are listed in Table I.

5. Coercive Force and Remanent Coercive Force at Room Temperature. [$H_c(T_0)$ and $H_{cr}(T_0)$].

In general, the coercive force of the ilmenite-hematite series is remarkably stronger than that of the titano-magnetite series [2], [15]. The variation with chemical composition of the coercive force and the remanent coercive force at room temperature is shown in Fig. 5. As observed in this figure, the coercive force decreases with the ilmenite content x fairly smoothly while the remanent coercive force shows a remarkable increase at $x \fallingdotseq 0.6$.

As stated already, the maximum magnetic field applied for the present measurements is only 800 *Oe.* which is obviously too weak to attain the saturation magnetization of the specimens, especially in the case of the parasitically ferromagnetic specimens. As a result, the values of H_c and H_{cr} in Fig. 5 and Table I are to be regarded as smaller than the ultimate coercivities. For example, the dependence of the coercive force on the intensity of the applied field of the specimen $x=0.01$ (hematite) is shown in Fig. 6. Extraporating the curve to the region of sufficiently strong magnetic field, the high coercivity of this substance reported by, for instance, R. Chevallier [17] may be expected.

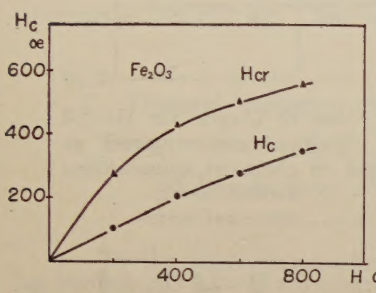

Fig. 6 Example of dependence of coercive force H_c and remanent coercive force H_{cr} on magnetic field applied.
Specimen : hematite ($x=0.01$)

6. Thermo-Remanent Magnetism. [$J^{T_0}_{T_c,\,2.0\ Oe.}(T_0)$]

The intensity of the total thermo-remanent magnetism (TRM) produced in a magnetic field of 2.0 *Oe.* is plotted in Fig. 7 against the chemical composition. In this figure, the values of TRM of the specimens of the *abnormal series* are also plotted by hollow cirlces. The most remarkable fact seen in this figure is that the specimens $x=0.56$ and $x=0.60$ show the "reverse thermo-remanent magnetism" (RTRM). Since the chemical composition of these specimens is close to that of the Haruna ferromagnetic ilmenite [7], the reverse TRM of the present artificial specimens may be presumed to have the same mechanism as that of the Haruna sample. It was, moreover, shown that the synthesized specimens of the ilmenite-hematite $x=0.45$, 0.48 and 0.51, can acquire the same type of reverse TRM by certain heat-treatment. The cross marks in Fig. 7 show the reverse TRM of the heat treated specimens. As for the reverse TRM, we will discuss in more detail in § 11.

Another remarkable feature of the TRM of the ilmenite-hematite series is its great intensity in the parasitically ferromagnetic region. For instance, the intensity of the TRM produced in the magnetic field of only 2.0 *Oe.* are comparable to, and some times greater than, the intensity of the induced magnetization in the magnetic field of 800 *Oe.* as seen in Tables I and II and in Figs. 10~17 and 21~23. This seems to be an important characteristic of the ilmenite-hematite series. To show this more

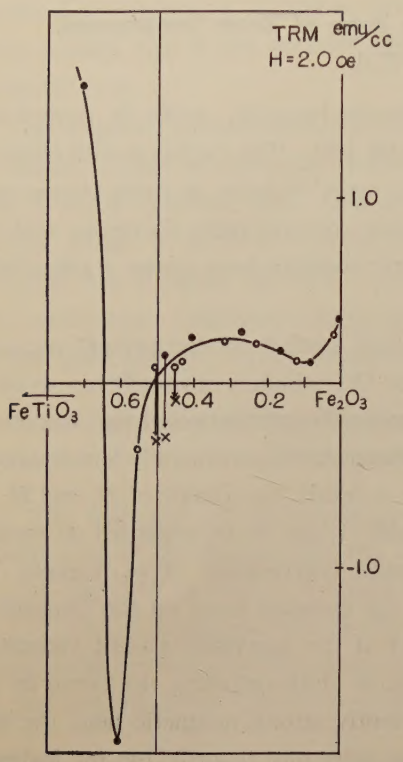

Fig. 7 Intensity of thermo-remanent magnetism at room temperature of ilmenite-hematite series as dependent on chemical composition: TRMs plotted are the total TRM produced by field-cooling in H=2.0 *Oe*.
• ....*normal series*, ○ ....*abnormal series*,
× ....after heat treatment (see text).

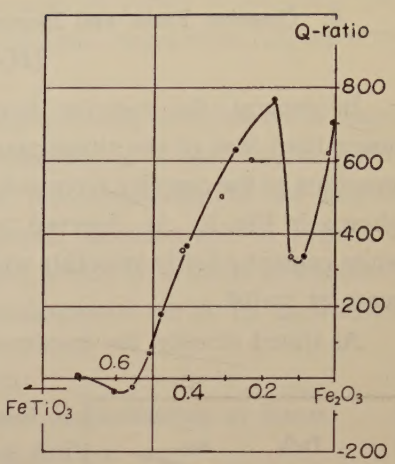

Fig. 8 Value of Q-ratio for H=2.0 *Oe*. of ilmenite-hematite series as dependent on chemical composition.
• ....*normal series*,
○ ....*abnormal series*.

clearly, the Q-ratio for H=2.0 *Oe*, defined as:

$$Q=\frac{\text{TRM}}{\text{induced magnetization}}$$

is plotted in Fig. 8 against the chemical composition. As seen in the figure and Tables I and II, the Q-ratio is over 200 in the parasitically ferromagnetic region, amounting nearly to 800 for the specimen $x=0.17$. For titano-magnetite series it has been known to be quite rare that Q-ratio exceeds 100 [12]. For the specimens having the characteristics of reverse TRM, the Q-ratio is of course negative.

The relation between the intensity of thermo-remanent magnetism and the coercive forces of the present specimens is shown in Fig. 9, in which roughly linear relations

$$J_{\text{TRM}} \propto H_c(T_0) \qquad (1)$$
$$J_{\text{TRM}} \propto H_{cr}(T_0) \qquad (1')$$

seem to be held. Relation [1] has been suggested by L. Néel for materials whose saturation magnetization and coercive force vary with temperature in a similar mode [13], and was experimentally verified by the present author for the ferromagnetic

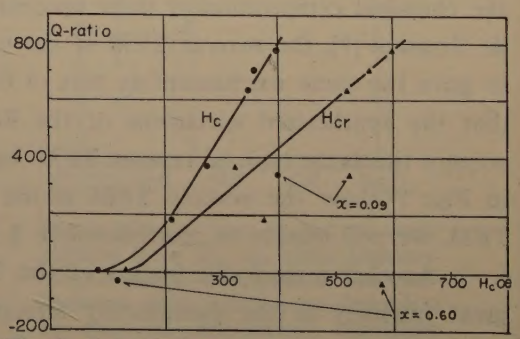

Fig. 9 Relation between Q-ratio for H=2.0 *Oe*. and coercive forces H_c and H_{cr} of ilmenite-hematite series.

ilmenites [7]. In the present cases, the modes of $J_s(T)$ and the temperature dependence of ultimate coercivities are not known for the magnetic field available is too weak. But, at least in the temperature range near the Curie point, the modes of $J(T)$ and of $H_c(T)$ or $H_{cr}(T)$ both seem to be linear as will be seen in Figs. 10～17.

In Figs. 8 and 9, in addition to the specimens having the Haruna-type reverse TRM, specimens $x \fallingdotseq 0.1$ can be noticed as not being included in the general tendency. In the ilmenite-hematite series, the specimen of this chemical composition seems to have some particular nature with regard to the thermomagnetic properties, which may, in the author's speculation, be related to the occurrence of the natural reverse remanent magnetism of the Adirondack ilmeno-hematites [8] and of the Allard Lake ilmenite-hematite deposits [9]. We will treat this in § 12.

7. Thermal Variation of Magnetization $J(T)$, Remanent Magnetization $J_r(T)$, Coercive Force $H_c(T)$, and Remanent Coercive Force $H_{cr}(T)$, and the Mode of Development of Thermo-Remanent Magnetism $J^{T_0}_{T_c,\ 2.0\ Oe}(T)$

In the preceding sections, the values measured at room temperature have mainly been considered. In this section, the modes of thermal variations of these quantities will be examined.

In Figs. 10～17 the results of the thermo-magnetic measurements on the specimens of the *normal series* are shown. In these figures, the symbols are as follows:

full circles connected by full curve....the magnetization $J(T)$ in the field of 800 *Oe*.

full circles connected by dotted curve....the remanent magnetization $J_r(T)$ produced by the field of 800 *Oe*.

hollow circles connected by full curve....the coercive force $H_c(T)$ after magnetized by the field of 800 *Oe*.

hollow circles connected by dotted curve....the remanent coercive force $H_{cr}(T)$ defined in Fig. 3.

cross marks connected by broken curve....the mode of the development of the total thermo-remanent magnetism $J^{T_0}_{T_c,\ 2.0\ Oe}(T)$.

The general tendency in the thermal variations in $J(T)$, and $J_r(T)$ of the parasitically ferromagnetic region of the ilmenite-hematite solid solution series can be characterized by their increase with the rise in temperature. This increase, being more remarkable for the hematite rich specimens, is considered to be a Hopkinson effect which is generally observed in the thermal variation of magnetization of ferromagnetic materials when measured in weak magnetic fields. For the parasitically ferromagnetic members of the ilmenite-hematite solid solution, having high coercivity, 800 *Oe*. is certainly a weak magnetic field. In Figs. 12～17, the increase in $J(T)$ and $J_r(T)$ is seen to be precisely accompanied by an also remarkable decrease in coercive forces. In this series, the coercive forces are seen to decrease with the rise in temperature in a rather simple manner. In the ferrimagnetic region (Figs. 10 and 11), where the coercive force

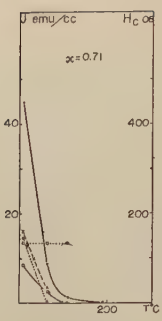

Fig. 10

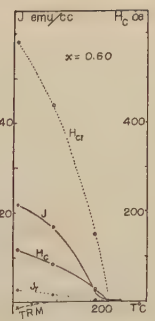

Fig. 11

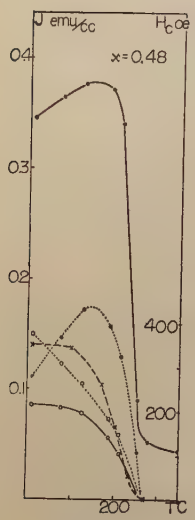

Fig. 12

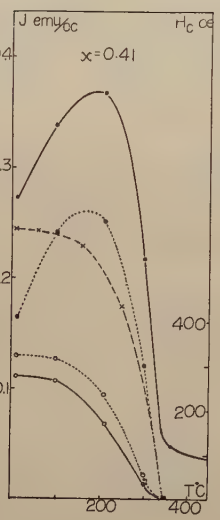

Fig. 13

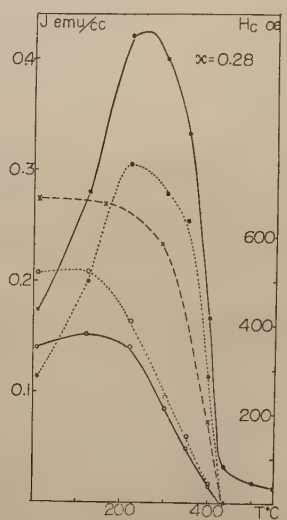

Fig. 14

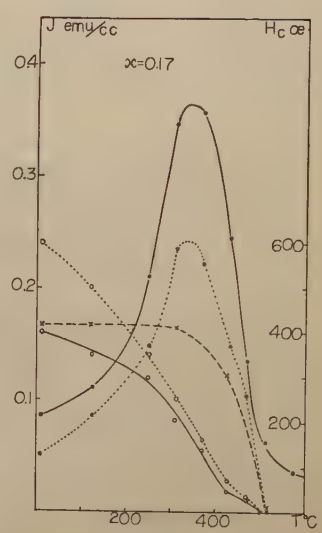

Fig. 15

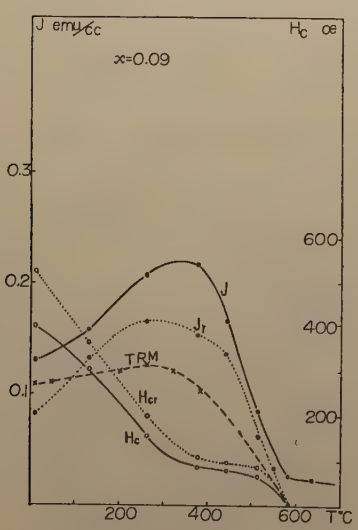

Fig. 16

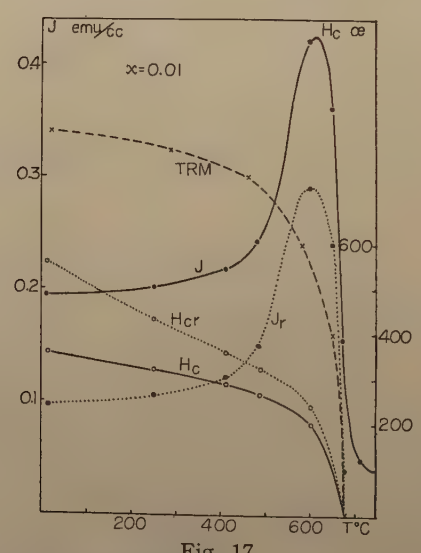

Fig. 17

Figs. 10–17 Thermal variation of magnetization J, remanent magnetization J_r, coercive force H_c and remanent coercive force H_{cr} of ilmenite-hematite series for H = 800 *Oe.* and the mode of development of thermo-remanent magnetism produced in H = 2.0*Oe.*

x-value....ilmenite content of specimen as expressed by $x\mathrm{FeTiO_3}\cdot(1\text{-}x)\ \mathrm{Fe_2O_3}$,

–•–•– .....magnetization J, ••••••• .....remanent magnetization J_r,

–o–o– .....coercive force H_c, ••o••o•• .....remanent coercive force H_{cr},

--×---×-- ..thermo-remanent magnetism.

is comparatively weak, the increase in $J(T)$ with the rise in temperature was not observed; $J(T)$ varied monotonously with the temperature like the natural ferromagnetic ilmenites [1].

The mechanism for the production of TRM has long been suggested by T. Nagata [12] as follows: fine grains of ferromagnetic mineral can acquire intense magnetization in a weak magnetic field at some critical temperature where the factors which hinder the free movement of magnetic domain walls, such as crystal anisotropy and magnetostriction, are diminished, and thus obtained magnetization can be fixed or frozen as the specimen is cooled to lower temperature in the same magnetic field. Néel put such idea of freezing of magnetization by weak-magnetic-field-cooling into more explicit forms [13]. In Néel's theories, the blocking of magnetic domains during field cooling from above the Curie point is presumed to take place at a temperature where the coercive force of the sample becomes equal to certain critical values; in one model the critical value is the externally applied magnetic field and in another model it is the thermal agitation field. In any case, it will be of significance to determine the relation between the critical temperature of thermo-remanent magnetism and the coercive force. Fig. 18 shows, for instance, the partial thermo-remanent magnetism characteristics and the coercive force of a specimen $x=0.01$ (hematite).

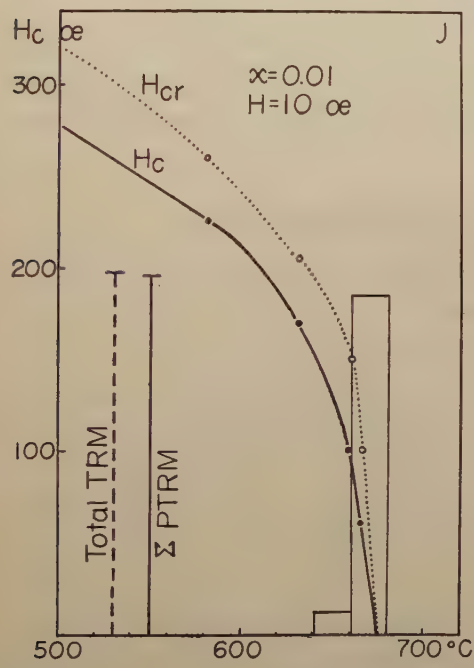

Fig. 18 Example of the spectrum of partial thermo-remanent magnetism $J_{T,\ 10\ Oe}^{T-20}(T_0)$ and thermal variation of coercive forces near the Curie point: specimen..hematite ($x=0.01$). Vertical lines at the left side of the figure represent the summation of the partial TRMs (full line), and the total TRM (broken line) respectively, indicating the validity of the *addition law of TRM.*

In this figure, it is clearly observed that the effective temperature range for the production of TRM is quite narrow and close to the Curie point; over 90% of the total TRM is produced in a temparature range of 20° including the Curie point. It is also found that in this range, the coercive force becomes of the comparable magnitude with the external magnetic field that is 10 *Oe.* in the present case. The addition law of TRM, [12], was also ascertained to be valid for this specimen as the figure shows.

8. Stability of Thermo-Remanent Magnetism of Ilmenite-Hematite Series against the Demagnetization by Alternating Magnetic Field.

Fig. 19 shows the demagnetization curves of TRM of the ilmenite-hematite series by alternating magnetic field. The TRM tested has been produced by a total magnetic field cooling in a magnetic field of 2.0 *Oe.* The ordinate, therefore, represents

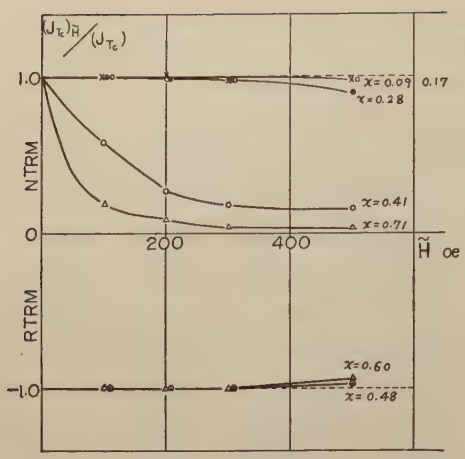

Fig. 19 Stability of thermo-remanent magnetism $J^{T_0}_{T_c,\ 2.0\ Oe}(T_0)$ of ilmenite-hematite series against demagnetization by alternating magnetic field $\tilde{H}$.

$(J_{Tc})_{\tilde{H}}/(J_{Tc})_{\tilde{H}=0}$ in the conventional notation [10]. In this figure, it is observed that the normal TRM of the ferrimagnetic samples ($x=0.71$ for instance) is not very stable against AC demagnetization, whereas the normal TRM of the parasitically ferromagnetic samples ($x<0.3$) and the reverse TRM are nearly completely stable.

In comparison with the similar curves for rocks containing titanomagnetite series reported by us previously [10], the stability of TRM of the parasitically ferromagnetic samples revealed in Fig. 19 is very high. This high stability of TRM is a natural consequence of the high coercive force of these samples.

It is a very remarkable fact that the reverse TRM of the ferrimagnetic specimen is as stable as the TRM of the parasitically ferromagnetic ones. In Fig. 19 the double circles show the reverse TRM of the specimen $x=0.48$ after heat-treatment (explanation in § 12).

9. Field Dependence of TRM of Ilmenite-Hematite Series.

Saturation phenomenon of TRM with the increase in the externally applied magnetic field has been recognized for rocks and bricks by various authors. T. Nagata empirically formulated this phenomenon by, [12],

$$J_{Tc} \propto \tanh kH, \qquad (2)$$

where k is a constant, and L. Néel provided a theoretical basis for it by a fine particle model [12]. Recently L. Néel proposed alternative expression for this phenomenon by multi-domain model as, [13],

$$\left.\begin{aligned} J_{Tc} &\propto H^{1/2} \\ J_{Tc} &\propto H \quad \text{(for weak fields).} \end{aligned}\right\} (3)$$

The field dependence of TRM of ilmenite-hematite series examined in the present study is shown in Fig. 20. Although either of the above expressions may be applicable in the present case when the magnetic field applied is smaller than some

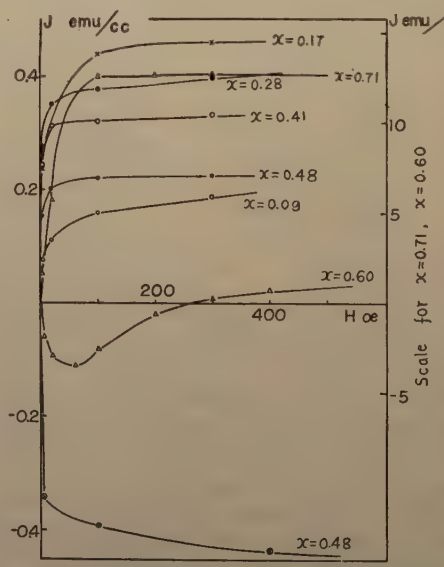

Fig. 20 Field dependence of thermo-remanent magnetism $J^{T_0}_{T_c,\ H}(T_0)$ of ilmenite-hematite series.

50 *Oe.*, the apparently perfect saturation of TRM for the field greater than some 100 *Oe.* shown in the figure is quite remarkable.

In this figure, it is also to be noticed that the specimens $x=0.60$ and $x\fallingdotseq 0.1$ are again of somewhat different nature from other specimens: their saturation effect is not as perfect as that of other specimens. The double circles again stand for the reverse TRM of the specimen $x=0.48$ after it acquired the reverse TRM characteristics by heat-treatment. It will especially be noteworthy that the specimen $x=0.48$ can retain its reverse TRM characteristics even in the field as intense as 500 *Oe.*, because this fact means that the effective magnetic field orienting the TRM of this sample in the reverse direction must overcome the normally directed external magnetic field of this strength. The bearings of this fact will be treated in § 11.

10. Summarized Results of the Specimens of the *Abnormal Series.*

So far, we have mainly referred to the experimental results obtained for the specimens of the *normal series.* In this section, the corresponding results on specimens of the *abnormal series* defined in § 2 will be reported briefly. Figs. 21～23, are the examples of the results of the thermo-magnetic measurements, where the symbols are identical with those in Figs. 10～17. Although the increase in $J(T)$ and in $J_r(T)$ with rise in temperature is similar to the case of the *normal series*, the increase in the coercive forces of the parasitically ferromagnetic specimens illustrated in Fig. 22 is in complete contrast to the case of the *normal series.* Among the specimens with $x<0.5$ of the *abnomal series*, only specimen $x=0.13$ (Fig. 23) did not show such increase in $H_c(T)$ and $H_{cr}(T)$. We have not yet found any plausible explanation for this increase of H_c and H_{cr}. The values of $J(T_0)$, $J_r(T_0)$, $H_c(T_0)$ $H_{cr}(T_0)$ and the Q-ratio are listed in Table II. Probably due to the above queer nature of the coercive force, such a simple relation between TRM and coercive forces as in Fig. 9 does not exist for this series. Fig. 24 shows the field dependence of TRM of the *abnormal series.* Nearly perfect saturation phenomenon of TRM is observed also for this series. The slower saturation for the specimens $x=0.56$ (RTRM) and $x\fallingdotseq 0.1$ is similar to the corresponding cases in Fig. 20. As was mentioned at the end of § 6, the specimens $x\fallingdotseq 0.6$ (reverse TRM) and $x\fallingdotseq 0.1$ showed the abnormal behaviours in TRM in the *normal series.* It is now clear that the same is true also for the *abnormal series.* (see also Fig. 7)

11. Reverse TRM Characteristics of Ilmenite-Hematite Series.

As stated already, some members of the ilmenite-hematite series show the reverse thermo-remanent magnetism. (see Table I.) In Fig. 25, the directions of TRM of the present specimens are shown by N (normal) and R (reverse) attached to the points representing the chemical composition of each specimens. As for the symbol R′, explanation will be given in § 12. The specimens with $x=0.60$ and 0.56 show a marked reverse TRM of which mode of development, shown in Figs. 11 and 21, is just similar to that of the reverse TRM of the natural ferromagnetic ilmenite

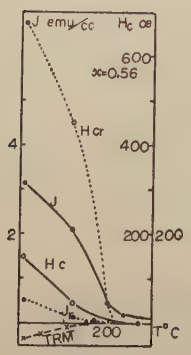

Fig. 21

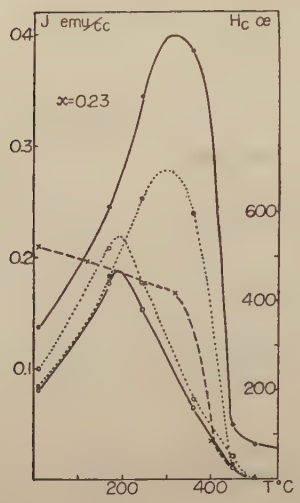

Fig. 22

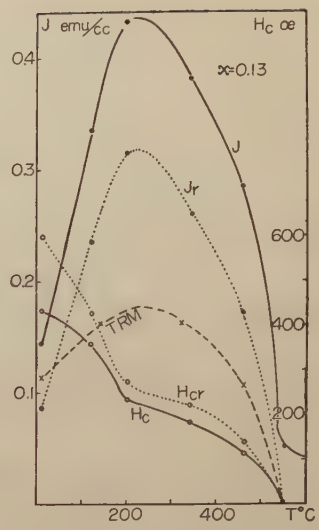

Fig. 23

Figs. 21–23 Examples of thermal variation of magnetization J, remanent magnetizaton J_r, coercive force H_c, remanent coercive force H_{cr} of the *abnormal* ilmenite-hematite series for H=800 *Oe.* and their mode of development of thermo-remanent magnetism produced in H=2.0*Oe.* Symbols are same as in Figs. 10–17.

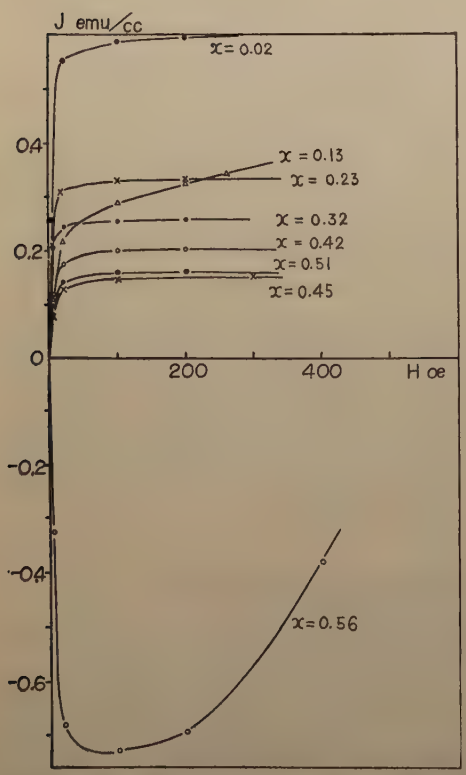

Fig. 24 Field dependence of thermo-remanent magnetism $J^{T_0}_{T_c,H}(T_0)$ of the *abnormal* ilmenite-hematite series.

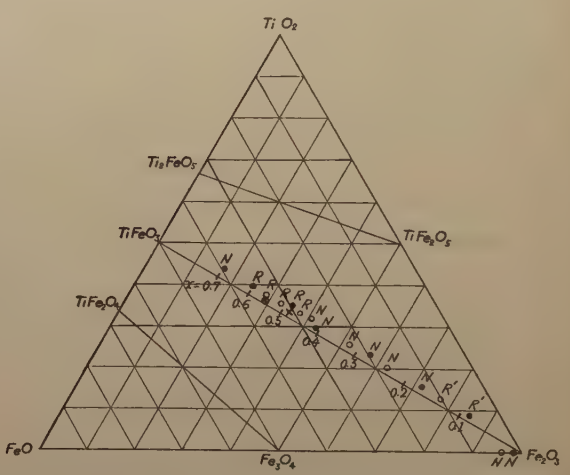

Fig. 25 Thermo-remanent characteristics of ilmenite-hematite series.
N....TRM in normal direction,
R....TRM in reverse direction (reverse TRM),
R'....tendency for reverse TRM,
• ....*normal series*, o ....*abnormal series*.
Double circle....Haruna sample

sample in the Haruna pumice [5]. Since the chemical composition of the natural ferromagnetic ilmenites which have the Haruna-type reverse TRM are known to be $x=0.6\sim0.5$, (double circle in Fig. 25 represents, for instance, the Haruna sample), it is quite probable that the reverse TRM of the specimens synthesized in the present study and the reverse TRM of the Haruna-type have a common origin. Since the specimens examined in the present study have been, during the process of synthesis, quenched from 1200°*C*, which definitely is above the top of the solvus curve of the ilmenite-hematite series [18], the two-phase hypothesis postulated hitherto [5] to explain the various characteristics of the Haruna-type reverse TRM must be reconsidered.

Moreover, the field dependence of the reverse TRM of the present specimens revealed in Fig. 20 indicates that the reverse TRM is still acquired by cooling in magnetic field as intense as 500 *Oe*. It can be readily shown that such an intense reverse magnetic field can hardly be accounted for by demagnetizing field in the conventional two-phase hypothesis [5].*

It seems likely that such intense reverse effective magnetic field may be caused by some coupling mechanism related to the Weiss-Heisenberg exchange forces.

In Fig. 7 or in Fig. 25, it is remarkable that the specimens showing the reverse TRM are concentrated in a limited region near the boundary between the ferrimagnetic and parasitically ferromagnetic regions of the ilmenite-hematite series: namely $0.45<x<0.6$. The magnetism of the specimens of this region has been noticed to be very sensitive to heat treatment [19], and on the basis of this sensitiveness on heat treatment, the production of ferromagnetism of the ilmenite-hematite series has been attributed to an ordering of *Ti* and *Fe* ions in the crystal lattice [4]. As mentioned in § 6, the characteristics of the reverse TRM has also been found to be sensitive to heat treatment. The best example of this is as follows.

The specimen denoted by a cross mark in Fig. 25 is a synthesized one from TiO_2, Fe_2O_3 and Fe in the same method as others and its chemical composition and the lattice parameters are:

FeO:	31.20 % in mol	$a_{rh}=5.471$ Å	
Fe_2O_3:	35.19 „	$\alpha_{rh}=55°05'$	
TiO_2:	33.61 „	∴	$x=0.48$

This specimen ($x=0.48$) was parasitically ferromagnetic and had only the normal TRM characteristics immediately after the synthesis. But, after being kept at 1000°*C* for 8 hours in an evacuated sealed quartz tube and slowly cooled, (this heat treatment is known to be effective in promoting the ordering for production of the ferrimagnetism of the specimen of this composition [19]), it became ferrimagnetic and acquired the reverse TRM characteristics. The reverse TRM of the specimens with $x=0.48$ in the *normal series* and $x=0.51$ and 0.45 in the *abnormal series* have also been acquired by the same

* For instance, the possible maximum demagnetizing field expected from an alternating parallel structure is $H_d=2\pi J$, where J is the saturation magnetization of the component with higher Curie point. For this value to exceed 500 *Oe.*, J must exceed 80 *emu/cc* whereas the saturation magnetization of our present samples is much smaller.

heat treatment, their original TRM being normal as shown in Figs. 7 and 12 and Tables I and II. It may be, therefore, well concluded that the production of the reverse TRM is closely related to the ionic ordering essential to the production of the ferrimagnetism of the ilmenite-hematite series. Since it is probable that the specimens in the boundary region between the ferrimagnetic and parasitically ferromagnetic regions contain both the ordered and disordered phases, the assumed Weiss-Heisenberg exchange interaction may be coupling these two phases, as in the case of Co and CoO reported by W.H. Meiklejohn and C.P. Bean [20].

Emphasis should, now, be placed on the fact that even purely artificial specimens show the reverse TRM. We shall discuss more fully on the mechanism of the reverse TRM in a forthcoming paper separately.

12. Imperfect Reverse TRM Characteristics of Ilmenite-Hematite Series.

The specimens with $x \fallingdotseq 0.1$ in both the *normal* and *abormal series* show an anomalous characteristic with respect to the mode of the development of TRM (cross marks in Figs. 16 and 23.). In an ordinary mode of the development of TRM, the TRM increases monotonoulsy with the decrease in temperature. But, the curves in Figs. 16 and 23 show that the TRM decreases from about 200°*C*. Although the TRM of these specimens at the room temperature is still normally directed, it definitely has a tendency for reverse TRM: such TRM will be called "imperfect reverse TRM" hereafter. The imperfect reverse TRM is denoted by R′ in Fig. 25.

That this tendency for reverse TRM is not caused by the presence of the component having the Haruna-type reverse TRM as impurity will be proved by the following experiment: in Fig. 26, the full and the hollow curves represent the mode of the development of the partial TRMs $J^{500°}_{570°}$, 100 *Oe* and $J^{250°}_{400°}$, 100 *Oe* respectively of the specimen $x=0.13$ (*abnormal series*). From these curves, it can be stated that the decrease of TRM, characteristic to the imperfect reverse TRM, takes place by the partial field-cooling in the high temperature range such as between 570°*C*-500°*C*, and not in the range between 400°*C*-250°*C*. The lower temperature range is known to be the effective range for production of the Haruna-type reverse TRM [5].

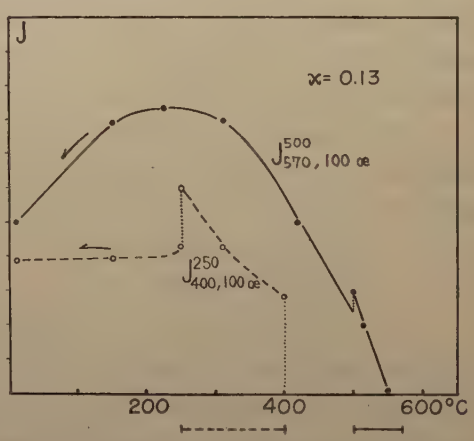

Fig. 26 Modes of development of partial thermo-remanent magnetisms $J^{500°}_{570°}$, 100 *Oe*. and $J^{150°}_{400°}$, 100 *Oe*. of the specimen $x=0.13$.

From this experiment, it is clear that for the production of the imperfect reverse TRM, the normally directed TRM of the phase having a Curie point at about 560°*C* is nesessary, and that the phase with lower Curie point is magnetized reversely by some

interaction with the already produced normal TRM of the high Curie point phase, which is the major constituent of the specimen $x \fallingdotseq 0.1$.

An alternative explanation for the phenomenon may be possible if we assume that the thermal variation of the saturation magnetization of the ilmenite-hematite series is Néel's P-type [21] at the composition $x \fallingdotseq 0.1$.

According to J.R. Balsley and A.F. Buddington [8], the magnetic minerals in the reversely magnetized rocks at Adirondacks are hematite rich ilmenite-hematite solid solutions with exsolution lamellae of ilmenite. The present author, therefore, considers that the natural reverse remanent magnetization of the Adirondack rocks may be caused by the similar mechanism as that of the imperfect reverse TRM of the present case, in the Adirondack rocks the extremely slow cooling in the process of metamorphism possibly having made the mechanism work so effectively as to bring about the perfect reversal of the remanent magnetism.

13. Conclusion

The thermo-remanent magnetism and the thermal variation of coercive force of the ilmenite-hematite solution series $(1-x)\,Fe_2O_3 \cdot x TiFeO_3$ have been investigated on synthesized specimens for the range $0<x<0.7$; the range $x>0.7$ has not been examined because the solid solution is known to be only paramagnetic in this range at room temperature. The range $0<x<0.7$ is known to be divided into two ranges: the ferrimagnetic range $0.7>x>0.5$ and the parasitically ferromagnetic range $0.5>x>0$ according to the intensity of magnetization. The magnetic characteristics investigated in the present study, such as the intensity and the thermal variation of the induced and remanent magnetization, of coercive forces, and of the thermo-remanent magnetism, were also found to be quite different in both ranges. In comparison with the ferrimagnetic range, the parasitically ferromagnetic range is characterized by the weak magnetization, high Curie point, high coercive force, high Q-ratio, and high stability of TRM against AC demagnetization.

With respect to the characteristics of the thermo-remanent magnetism, the border range $(0.45<x<0.6)$ between the ferrimagnetic and parasitically ferromagnetic ranges is quite conspicuous for the occurrence of the reverse thermo-remanent magnetism.

The specimens with $x \fallingdotseq 0.1$ are also remarkable because it shows a definite tendency for reverse TRM.

The ilmenite-hematite solid solution is, thus, quite important in rock-magnetism because of these various abnormal thermo-remanent characteristics of which origin is, from various experimental results, considered to be closely related with the very fundamental nature of the magnetism of this series itself. Further studies are under progress along this line.

In concluding, the author would like to express his deepest gratitude to Prof. T. Nagata for his kind directions throughout the course of this study. He also wishes to thank Dr. T. Rikitake for his encouragement, to Dr. S. Akimoto, Dr. S. Iida and Mr. Y. Ishikawa of Tokyo University for their valuable discussions and to Mr. M.

Ozima, now at University of Toronto, for the construction of the apparatus for the measurement. For the chemical analysis of the synthesized specimens, the writer is wholly indebted to Dr. K. Katsura of Tokyo Institute of Technology.

References

[1] Nagata, T., Akimoto. S. and Uyeda, S.: Journ. Geomag. Geoele. **5**, 168 (1953)
[2] Nagata, T. and Akimoto. S.: Geofisica pura e applicata, **34**, 36 (1956)
[3] Bizette, H. et Tsai, B.: Comptes Rendus, **242**, 2124 (1956)
[4] Ishikawa, Y. and Akimoto, S.: Journ. Phys. Soc. Japan, **12**, 1083 (1957)
[5] Uyeda, S.: Journ. Geomag. Geoele., **7**, 9 (1955)
[6] Nagata, T. and Uyeda, S.: Nature, **177**, 179 (1956)
[7] Uyeda, S.: Journ. Geomag. Geoele., **8**, 39 (1956)
[8] Balsley, J. R. and Buddington, A. F.: Iourn. Geomag. Geoele., **6**, 176 (1955)
[9] Hammond, P.: Economic Geology, **47**, 634 (1952)
[10] Nagata, T., Akimoto, S., Uyeda, S., Momose, K. and Asami, E.: Journ. Geomag. Geoele., **6**, 182 (1955)
[11] Roquet, J.: Ann. Géophysique, Tome 10, 226, 282 (1954)
[12] Nagata, T.: Rock-Magnetism, Maruzen, Tokyo (1953)
[13] Néel, L.: Phil. Mag. Suppl., **4**, 191 (1955)
[14] Nagata, T., Uyeda, S. and Akimoto, S.: Journ. Geomag. Geoele., **4**, 22 (1952)
[15] Deutsch, E. R.: Journ. Geomag. Geoele, **8**. 108. (1956)
[16] Akimoto, S.: Thesis, Tokyo University, (1957)
[17] Chevallier, R.: Journ. Physique et Radium, Tome 12, 172 (1951)
[18] Uyeda, S.: to be published
[19] Ishikawa, Y. and Akimoto. S.: Journ. Phys. Soc. Japan, **12**, 834 (1957)
[20] Meiklejohn, W.H. and Bean, C.P.: Phys. Rev., **102**, 1413 (1956)
[21] Néel, L.: Ann de Physique, **3**, 137 (1948)

Solar Activity and Cosmic Radiation

By Robert R. BROWN*

Department of Physics, University of New Mexico
(Albuquerque, New Mexico)

(Read on Oct. 10, 1957; Received on Oct. 21, 1957)

Abstract

Observations on the correlation of solar activity and cosmic radiation are reported. The relation of these results to models involving solar corpuscular streams is briefly conidered.

Introduction

Investigations of the time variations of cosmic radiation have established a connection between some aspects of solar activity and cosmic radiation; in particular, it has been found that a few large solar flares are accompanied by large but brief intensity increases on the earth and on some occasions are followed by decreases, together with magnetic storms.[1] In addition to these variations, evidence has been obtained which indicates that there are variations associated with the 27-day period of solar rotation[2] as well as the 11-year period of the solar cycle.[3]

Since the solar flare component as well as the main component, presumably of galactic origin, approach the earth through the solar system, both components of cosmic radiation are subject to the influence of interplanetary magnetic fields. Thus, the electromagnetic conditions in the solar system are expected to be reflected in such experimental observations as the rate of rise and fall of flare radiation, the 27-day and 11-year variations.

In this connection, recent investigations[4-8] have examined questions relating to the source, nature and role of interplanetary magnetic fields in cosmic ray effects. The fields considered in these discussions have their origin in the galaxy as a whole or on the sun and are turbulent in nature, due to either the pressure of solar corpuscular radiation or the hydromagnetic transport of solar fields. Field configurations which have been treated include 1) a field-free cavity,[4] swept out by solar streams, with walls made up of lines of force of the galactic field, 2) turbulent solar streams of magnetized gas clouds[5-7] and 3) spherical shells[8] of tangled or disordered fields centered on the sun. Whichever model is finally adopted, it must satisfy certain specific cosmic ray requirements: 1) allow relatively direct orbits connecting the sun and the earth so as to provide a means whereby the rise of flare radiation at the earth may be fairly rapid, yet 2) provide some means to explain the slow decay of

* Now at the University of California, Berkeley, California.

flare radiation and further 3) provide modulating mechanisms to account for the 27-day and 11-yeay variations. Other requirements involve astrophysical considerations: the model must avoid 1) degrees of symmetry which cannot be maintained in nature and 2) excessive drains on solar resources in the form of corpuscular emission and magnetic fields.

While the details remain to be worked out, the model[5-7] involving magnetized streams emanating from the equatorial regions of the sun appears to offer promise. For this configuration the drain on solar resources is reduced considerably and the geometry is consistent with the known features of solar activity. In addition, some progress has been made with this model toward understanding flare effects by considering the diffusion of particles through magnetized gas clouds and modulation effects by considering the capture and support of magnetized gas clouds by the earth's gravitational and magnetic fields.

It is the purpose of this paper to present experimental observations during a period of intense solar activity which may have bearing on these questions; in particular, to consider the relation of solar activity and slow cosmic ray variations as shown in the period surrounding the 1956 flare outburst.[9]

Observations

A. Recent Event

Forbush[8] has published the results of a long-term study of the variations of cosmic ray intensity registered by Compton-Bennett ionization chambers. The data obtained during the period 1937–1952 show that there was a variation of cosmic ray intensity over the 11-year solar cycle, annual means of cosmic ray intensity displaying a negative correlation with sunspot number. In this study the possible influence of short term magnetic disturbances was examined by comparing the variation of annual means for all days, international magnetic quiet and disturbed days. The results of this comparison indicate that variations of intensity with sunspot number persist for periods longer than those characteristic of transient magnetic disturbances.

Kodama and Murakami[10] have published results of neutron intensity observations at Nagoya for the interval September 1954 to August 1955. Their observations, although obtained near solar minimum, also indicate a negative correlation of cosmic ray intensity with sunspot number.

Since it has been established that a linear relationship connects long-term averages of sunspot numbers and areas, a correlation similar to that with snnspot number is expected to exist between cosmic ray intensity and sunspot area. In addition, it is to be expected that the *size* of sunspots would be more closely related to solar-terrestrial effects than number, especially during periods of intense solar activity lasting times short compared to the length of the solar cycle. In view of these points, it is of interest to consider the solar cosmic ray outburst of February 23, 1956 which was preceded by very intense solar activity.

Observations of the cosmic ray intensity variations surrounding this event,[12] obtained with a neutron monitor, indicate a close time-association between the daily averages of cosmic ray intensity, corrected for barometric fluctuations, and the disk passage of active regions on the sun. In addition, examination of sunspot data[13] for this period, as shown in Fig. 1, indicates that the cosmic ray intensity was negatively correlated with sunspot area, at least for the months of January and February.

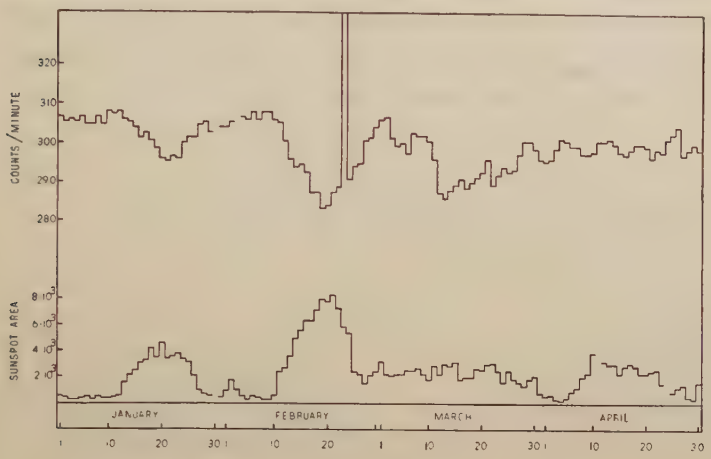

Fig. 1 Cosmic Ray Intensity (nucleonic component) and Sunspot Area for the Period January-April 1956 (Area expressed in millionths of the sun's hemisphere and corrected for foreshortening).

The role of transient magnetic disturbances is more difficult to determine in a short-term study such as with this event. One possible approach is to indicate the magnetically quiet and disturbed days[14] during the period and examine their distribution relative to the cosmic ray variations. These days are given in Table. 1 and are indicated by Q (quiet) and D (disturbed). Inspection of the data in Fig. 1 shows that for the months of January and February the intensity variations were relatively slow, both during the decreasing and increasing phases. Further, the distribution of Q and D-days given in Table. 1 does not show any unusual trends which might suggest that the variations were due to the superposition of a number of transient magnetic storm effects; rather, it is seen that Q-days are found to occur while the intensity was decreasing and D-days while it was increasing.

For the months of March and April, following the cessation of intense solar activity, the cosmic ray intensity variations were of a different character; instead of a slow decline and recovery, lasting about 14 days, the intensity decreased rapidly over two or three days and then recovered slowly, over a period of 45 days, with brief variations super-

Table 1. *Magnetically quiet and disturbed days.*[14]

Month	Q (quiet days)	D (disturbed days)
January	8	11
	15	18
	16	19
	20	24
	26	28
February	7	11
	8	12
	9	25
	10	28
	14	29
March	7	3
	8	21
	9	22
	17	24
	18	29
April	13	21
	14	22
	15	27
	24	28
	25	30

imposed. These variations are probably related to the next disk passage of the active regions responsible for the variations in January and February. Toward the end of April an intense geomagnetic storm occured; this storm, in contrast to the magnetic disturbances which occured earlier,[12] produced the familiar rapid decrease and recovery in intensity.

Just as the intensity variations for March and April differ from those in January and February, so does the correlation between intensity and sunspot area. Thus, inspection of Fig. 1 shows the sunspot area considerably above the minima for January and February but in poor correlation with the intensity variations.

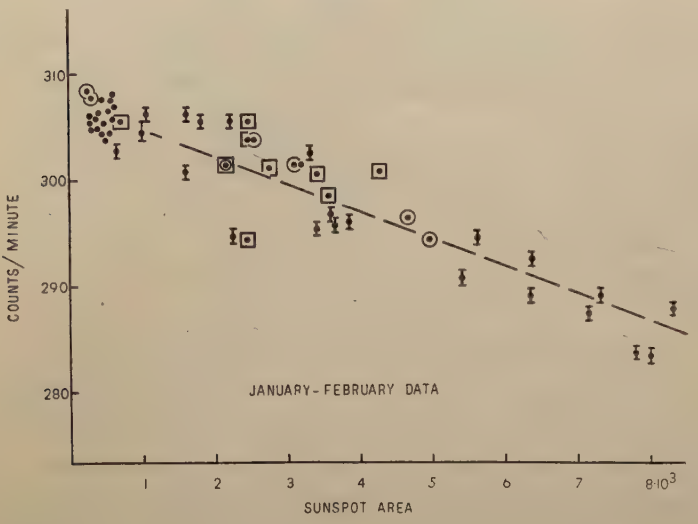

Fig. 2 Cosmic Ray Intensity (nucleonic component) and Sunspot Area (expressed in millionths of the sun's hemisphere) for the Months of January and February 1956.

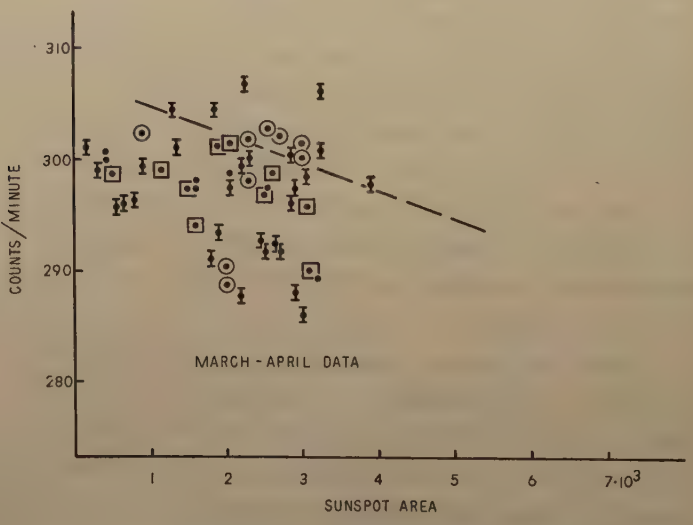

Fig. 3 Cosmic Ray Intensity (nucleonic component) and Sunspot Area (expressed in millionths of the sun's hemisphere) for the Months of March and April 1956.

Another presentation of the January-February and March-April neutron data is given in Figs. 2 and 3, where cosmic ray intensity is plotted against sunspot area. The distinction between the two periods is evident from these plots; the January-February data show a rough linear correlation over a wide range of solar activity

whereas the March-April data show considerable scatter and deviation below the correlation line. In these plots the magnetically quiet (Q) and disturbed (D) days are represented by circles and squares, respectively; it is seen that their distribution does not show any pronounced trends.

Cosmic ray intensity observations obtained with an ion chamber located at the geomagnetic equator[15] (Huancayo, Peru) also show the intensity variations described above. A presentation of the 1956 ion chamber data, similar to that given for the neutron monitor data, is shown in Fig. 4. While the ion chamber observations resemble rather closely those obtained with the neutron monitor, it is seen that the amplitude of the variations is considerably smaller. This is due to the location of the detector at a low geomagnetic latitude and the fact that the ion chamber responds mainly to the mu-meson component which has a higher mean primary energy than the nucleonic component.

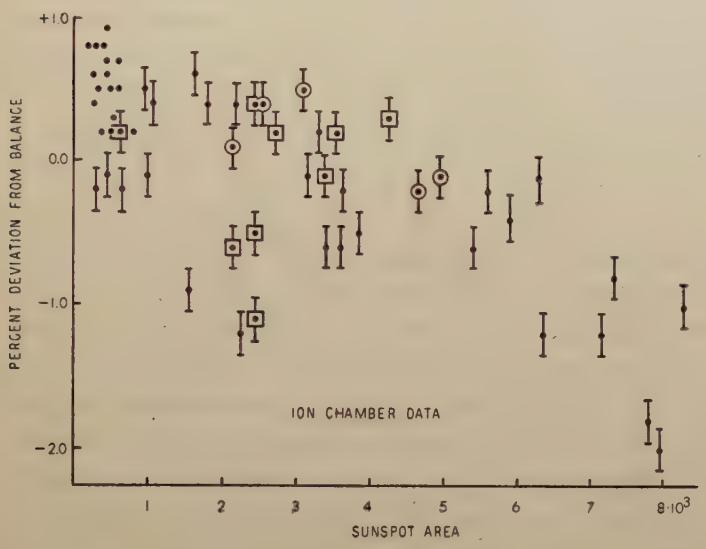

Fig. 4 Cosmic Ray Intensity (meson component) and Sunspot Area (expressed in millionths of the sun's hemisphere) for the Months of January and February 1956.

B. Previous Events

Four solar cosmic ray outburst of the type observed on February 23, 1956 have been observed earlier: February 28, 1942, March 7, 1942, July 26, 1946 and November 19, 1949. With the exception of the November 19, 1949 event,[16] all previous events have been observed with Geiger counter telescopes or ion chambers. As mentioned above, these devices respond mainly to the mu-meson component for which the average primary energy, at a given geomagnetic latitude, is considerably greater than that for the nucleonic component. It has been found in the case of these events that flares produced increases in intensity of the order of 30% in such detectors; in addition, the increases were followed by a slow decay lasting seveal hours after the flares. However, in contrast to the 1956 event, no increases were observed at the geomagnetic equator. Intensity decreases due to magnetic disturbances following some of the flares, on the other hand, were world-wide, being observed at middle as well as low geomagnetic

latitudes.

It would be of interest to examine the data[3] for these earlier events for modulation effects similar to those observed prior to the 1956 event. Unfortunately, the ion chamber data[15] and the solar activity data,[17] while not inconsistent with solar-controlled downward modulation, do not show clear-cut intensity decreases for these events. Considering the amplitude of the variations at Huancayo in the case of the 1956 event and the fact that the solar activity preceding the earlier events was less intense and of shorter duration (expressing sunspot area in millionths of the visible hemispher, $A_{max}\sim2500$ for the 1942 events, $A_{max}\sim5000$ for the 1946 event and $A_{max}\sim3500$ for the 1949 event), this result is not unexpected.

Discussion

One feature common to all the flare events is the slow decay of post-flare radiation. At the present time there seems to be two possible explanations of this feature: either a continuous but gradually decreasing emission of flare particles, extending beyond the duration of the visible aspects of the flares, or the trapping and leakage of flare particles out of an interplanetary field. Of the five outbursts, the 1956 event has been studied in the greatest detail. Experimental data[8,18] on the distribution of the post-flare radiation for this event indicates that it had a rather high degree of isotropy and thus argues against the continuous emission of particles by the sun.

Whether the interplanetary magnetic field, required by the above discussion, has a relatively permanent existence or is occasionally transported out from the sun by streams resulting from enhanced solar activity, is not clear from observations of earlier flare events. However, the striking correlation of cosmic ray intensity with sunspot area and disk passage of active regions in January and February strongly suggests that, in this case, these decreases find their explanation in modulation effects produced by magnetized solar streams. These observations seem consistent with a geocentric model involving the interaction of the earth's magnetic field with a broad solar stream, perhaps along the lines indicated by Parker[6] where modulation effects are ascribed to the capture and support of additional magnetized clouds sent out from the sun by the earth's gravitational and magnetic fields. Within the framework of this interpretation the sunspot area of the visible hemisphere would give a measure of the density of the streams emanating from the sun from which clouds are captured by the earth. However, the duration of the decreases would be related to the details of the capture and retention of clouds from the streams. In view of the fact that the intensity variations follow the solar activity rather closely, it would appear that the clouds captured by the earth's gravitational field are not bound very strongly by the earth. In developing an explanation of this feature, it would seem that capture of clouds would play a dominant role while the solar stream is overtaking and enveloping the earth while the loss of clouds through collisions with clouds in the stream would become important after the earth has passed through the more central portions of the stream.

Acknowledgements

The author is indebted to Dr. Scott E. Forbush of the Department of Terrestrial Magnetism, Carnegie Institution of Washington, for providing the Huancayo ionization chamber data. The neutron monitor observations were supported by a Frederick Gardner Cottrell Grant from the Research Corporation.

References

[1] S. E. Forbush and I. Lange, Carnegie Inst. Wash., Pub. 175, (1948).
[2] J. A. Simpson, Phys. Rev., **94,** 426, (1954).
[3] S. E. Forbush, J. Geophys. Research., **59,** 525, (1954).
[4] L. Davis, Phys. Rev., **100,** 1440, (1955).
[5] R. R. Brown, J. Geophys. Research., **62,** 147, (1957).
[6] E. N. Parker, Phys. Rev., **103,** 1518, (1956).
[7] K. Kawabata, I. Kondo, K. Murakami and M. Wada (1957 IUPAP Cosmic Ray Conference).
[8] P. Meyer, E. N. Parker and J. A. Simpson, Phys. Rev., **104,** 768, (1956).
[9] T. Gold and H. Elliot, Collection of Cosmic Ray, Solar, Ionospheric and Magnetic Data relating to the Solar Cosmic Ray Outburst 23 February 1956, Royal Greenwich Observatory.
[10] M. Kodama and K. Murakami, J. Geomag. and Gecelec., Vol. VIII, No. **2,** 71, (1956).
[11] K. O. Kiepenheur, Chapter 6, "The Sun", edited by G. Kuiper, University of Chicago Press, (1953).
[12] R. R. Brown, J. Geophys. Research., **61,** 639, (1956).
[13] Positions, Areas and Counts of Sunspots, U. S. Naval Observatory Circular.
[14] Solar-Geophysical Data, Series F, Part B, Central Radio Propagation Laboratory, National Bureau of Standards.
[15] S.E. Forbush, private communication.
[16] N. Adams, Phil. Mag., **41,** 503, (1950).
[17] Monthly Weather Review, U. S. Department of Commerce.
[18] G. Pfotzer, Mitteilungen aus dem Max Planck Institut für Physik der Stratosphäre, Weissenau bei Ravensburg, Nr. 7, (1956).

Horizontal Wind Systems in the Ionospheric E Region Deduced from the Dynamo Theory of the Geomagnetic S_q Variation Part III

By Hiroshi MAEDA

Department of Earth Science, Yoshida College, Kyoto University

(Read July 5, 1957; Received July 10, 1957)

Abstract

In Parts I and II ionospheric wind systems have been deduced from the geomagnetic S_q variations for the mean solstice. In order to compare our results with observation, however, it is still necessary to obtain the wind systems for the solstitial seasons. In this paper wind systems in summer and winter hemispheres are deduced from the S_q data. It is shown that the diurnal wind component has greater magnitude in summer than in winter; whereas the semi-diurnal component has smaller magnitude in summer than in winter over most of the hemisphere, and that in summer hemisphere the diurnal wind component is greater than the semi-diurnal one; whereas in winter hemisphere the former is more or less smaller than the latter. A comparison between our results and observed ionospheric winds is made.

1. Introduction

In Part I (by this author [1]) and Part II (by S. Kato [2]) of this report we have obtained the horizontal wind systems in the ionospheric E region from the dynamo theory of the geomagnetic S_q variation, and it has been found that the main component of winds required to produce the S_q variations is not semi-diurnal, but diurnal. M. Hirono and T. Kitamura [3] have also treated this problem on some different assumptions, and obtained the results similar to ours. Since all these works [1,2,3] are based on geomagnetic data for the mean solstice, the results seem to represent a mean state of summer and winter. In order to compare the calculated results with observation, it is, therefore, still necessary to obtain the wind systems for each of both solstitial seasons. In the present paper (Part III) the wind systems in Northern summer and winter (i.e. Southern winter and summer, respectively) are deduced from the geomagnetic data by a similar method to in Part I, on the assumption, for simplicity, that the motion of the air in regions concerned is horizontal and irrotational. Further extension of Part III, taking into account the effect of the Coriolis force, will be made in Part IV by Kato [4].

The data used are the horizontal intensity of the geomagnetic S_q variations at 62 stations over the world in summer and winter of the Second Polar Year, 1932-33. The

harmonic coefficients of the North (ΔX) and East (ΔY) components of S_q are plotted in Fig. 1. The full (for Northern summer) and dotted (for Northern winter) lines in this figure show a smooth distribution of the coefficients derived from the potential of the S_q field for the mean solstice [5] and solstitial difference [6] (see Table 1), on the assumption that the mean solstitial field of S_q is symmetrical, and that the solstitial-difference field is anti-symmetrical with respect to the equatorial plane. Since the spherical harmonic coefficients shown in Table 1 are obtained from the S_q data in the interzonal region (between 60°N and 60°S), the high-latitude curves in Fig. 1 are an extraporation of S_q in middle and low latitudes.

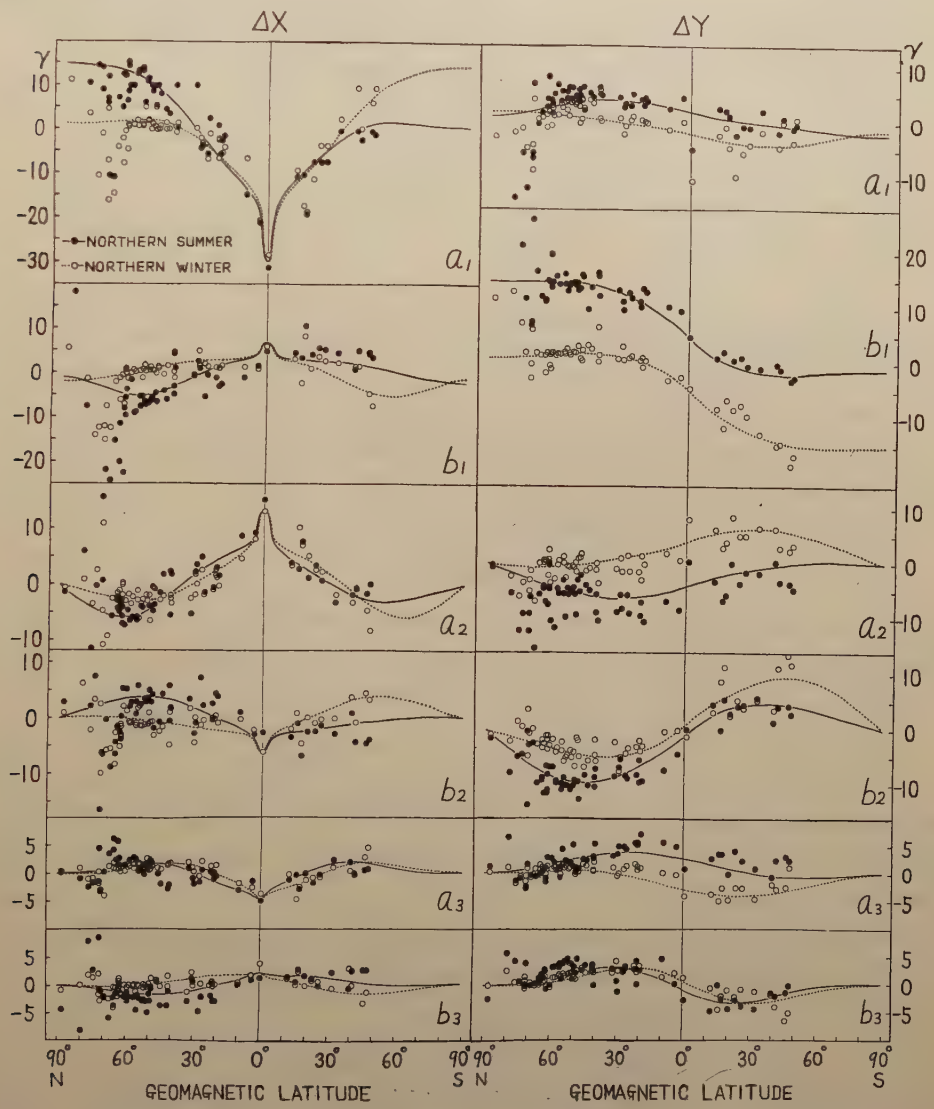

Fig. 1 Latitude-distributions of the harmonic coefficients for the geomagnetic North (ΔX) and East (ΔY) components of the geomagnetic S_q variations in summer and winter. The full (for Northern summer) and dotted (for Northern winter) lines show a smooth distribution obtained from the spherical harmonic coefficients listed in Table 1.

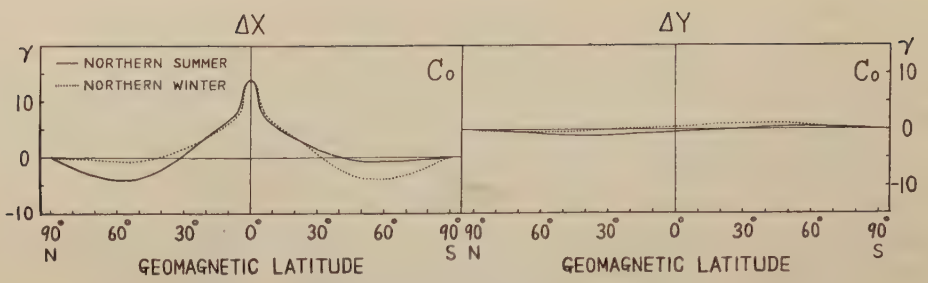

Fig. 2 Latitude-distributions of the constant term C_0.

Table 1. Spherical harmonic coefficients for the mean solstitial and solstitial-difference fields of S_q in the interzonal region (between 60°N and 60°S) analyzed in the form

$$V=r_0\sum_n\sum_m(a_n^m\cos mt+b_n^m\sin mt)P_n^m(\cos\theta),$$

using the Second Polar Year data. (Unit=γ)

		$\frac{1}{2}(S+W)$			$\frac{1}{2}(S-W)$	
m	n	a_n^m	b_n^m	n	a_n^m	b_n^m
1	2	8.40	−2.35	1	5.41	−1.90
	4	−1.75	0.40	3	0.82	0.43
	6	0.21	0.12	5	−0.14	0.34
2	3	−4.15	1.69	2	−0.88	2.38
	5	0.14	−0.15	4	−0.67	0.03
	7	−0.02	0.22	6	−0.10	−0.08
3	4	1.42	−0.86	3	−0.19	−1.16
	6	0.30	−0.02	5	0.27	0.04

2. Method

In this paper, the dynamo equation eliminating the velocity potential is used. Omitting unnecessarily detailed descriptions (see [1] or [3]) we have

$$\frac{\partial^2 S}{\partial\theta^2}+\frac{1}{\sin\theta\cos\theta}\frac{\partial S}{\partial\theta}+\frac{1}{\sin^2\theta}\frac{\partial^2 S}{\partial\lambda^2}=-a\left\{\frac{\partial E_x}{\partial\theta}+\frac{E_x}{\sin\theta\cos\theta}+\frac{1}{\sin\theta}\frac{\partial E_y}{\partial\lambda}\right\}$$
$$\equiv F(\theta,\ \lambda), \qquad (1)$$

where S is the electrostatic potential; θ, λ the colatitude and east longitude, respectively; a the radius of a current sheet; E_x, E_y the Southward and Eastward components of the total electric field.

The right-hand side of (1) can be calculated, if the total electric field $\boldsymbol{E}$ is known. This field is approximately estimated from the relation

$$\left.\begin{aligned} I_x\left(\simeq\frac{\Delta Y}{2\pi}\right)&=\Sigma_{xx}E_x+\Sigma_{xy}E_y,\\ I_y\left(\simeq\frac{\Delta X}{2\pi}\right)&=-\Sigma_{xy}E_x+\Sigma_{yy}E_y,\end{aligned}\right\} \qquad (2)$$

using the geomagnetic North (ΔX) and East (ΔY) components of S_q, corrected by the constant term C_0 (see Fig. 2), and the height-integrated conductivities given by the form [7]

$$\begin{Bmatrix} \Sigma_{xx} \\ \Sigma_{yy} \\ \Sigma_{xy} \end{Bmatrix} = \begin{Bmatrix} \Sigma_{xx0} \\ \Sigma_{yy0} \\ \Sigma_{xy0} \end{Bmatrix} (1+2.00\cos\chi+1.46\cos^2\chi),$$

where

χ = solar zenith angle.

The total field for the Northern summer (i.e. Southern winter) is shown in Fig. 3.

Thus the differential equation (1) for the electrostatic potential S can be solved. The boundary conditions satisfied by S are: S must vanish at the poles, and the static field derived from S is equal to the total field at the equator, because the dynamo field vanishes there.

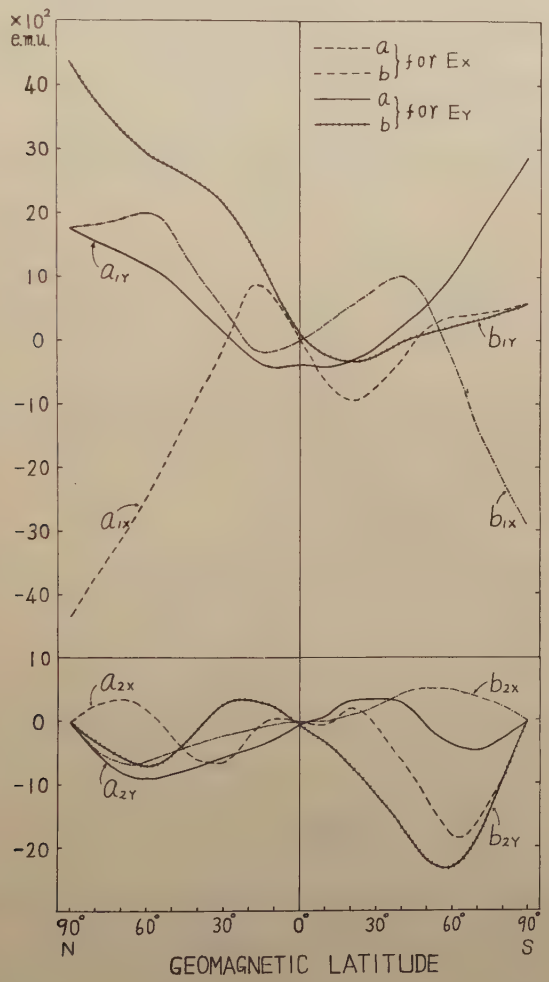

Fig. 3 Latitude-distributions of the harmonic coefficients for the total electric field components E_x, E_y in Northern summer.

3. Solution of the Differential Equation

The right-hand side of (1) calculated by using the total field obtained above is expressed as follows:

$$F(\theta, \lambda)=\sum_m \{f_{ma}(\theta)\cos m\lambda+f_{mb}(\theta)\sin m\lambda\}.$$

If we put

$$S(\theta, \lambda)=\sum_m \{s_{ma}(\theta)\cos m\lambda+s_{mb}(\theta)\sin m\lambda\},$$

then (1) is reduced to

$$\left.\begin{aligned}&\frac{\partial^2 s_{ma}}{\partial\theta^2}+\frac{1}{\sin\theta\cos\theta}\frac{\partial s_{ma}}{\partial\theta}-\frac{m^2}{\sin^2\theta}s_{ma}=f_{ma}(\theta),\\&\frac{\partial^2 s_{mb}}{\partial\theta^2}+\frac{1}{\sin\theta\cos\theta}\frac{\partial s_{mb}}{\partial\theta}-\frac{m^2}{\sin^2\theta}s_{mb}=f_{mb}(\theta).\end{aligned}\right\} \qquad (3)$$

The general solution of (3) consists of a particular solution and complementary functions. A particular solution $s_{m(p)}$ is obtained by means of numerical integration. The homogeneous equation of (3) is reduced to the hypergeometric equation by the same substitutions as in Part I. One of linearly independent solutions of this equation tends to infinity as $\theta\to 0$, hence only the following solution is adopted:

$$s_{m(c)}=\sin^m\theta F\left(\frac{m}{2},\ \frac{m}{2};\ m+1;\ \sin^2\theta\right),$$

where $F(a, b; c; z)$ stands for the hypergeometric function. The general solution is, therefore, given by

$$s_m=s_{m(p)}+C\,s_{m(c)},$$

where C is an integration constant. Since both particular and complementary solutions satisfy the conditions at the poles, the value of integration constant C can be determined by the condition at the equator, consequently the unique solution is obtained. Further detailed descriptions of the method of obtaining the solution will be given in Part IV by Kato [4].

4. Results

The static field $\boldsymbol{E}_s$ is derived from the potential S as follows:

$$E_{sx}=-\frac{\partial S}{a\partial\theta},\qquad E_{sy}=-\frac{\partial S}{a\sin\theta\,\partial\lambda},$$

and subtraction of this field from the total field gives the dynamo field $\boldsymbol{E}_i$. Thus the wind velocity is calculated from the dynamo field by the relation

$$u=-\frac{E_{iy}}{H_z},\qquad v=\frac{E_{ix}}{H_z},$$

where H_z is the vertical component of the geomagnetic intensity. The resultant distributions of the wind velocity are illustrated in Figs. 4 and 5 for each of Northern summer and Northern winter. The wind vectors of the diurnal and semi-diurnal components shown in Figs. 4 and 5 are also plotted in Fig. 6 in polar form, for convenience of comparison with observation.

From these figures the following will be seen:

(*a*) *Diurnal wind component*

1) The 24-hourly harmonics represent a clockwise rotation in the Northern hemisphere, and an anticlockwise rotation in the Southern hemisphere. 2) The movement

is towards the North (South) at 1500 hr in summer in the Northern (Southern) hemisphere, and at 1100 hr in winter in the Northern (Southern) hemisphere. 3) The magnitude of the rotating vectors is about 40 m/sec in summer, and about 15 m/sec in winter,

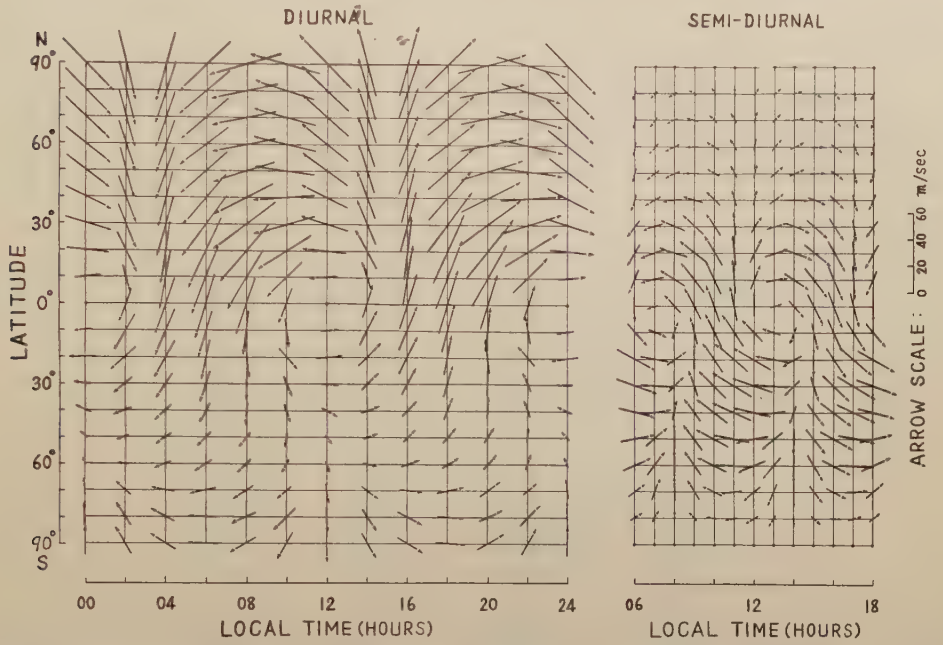

Fig. 4. Distributions of the wind velocity in Northern summer for each of the diurnal (left) and semi-diurnal (right) components.

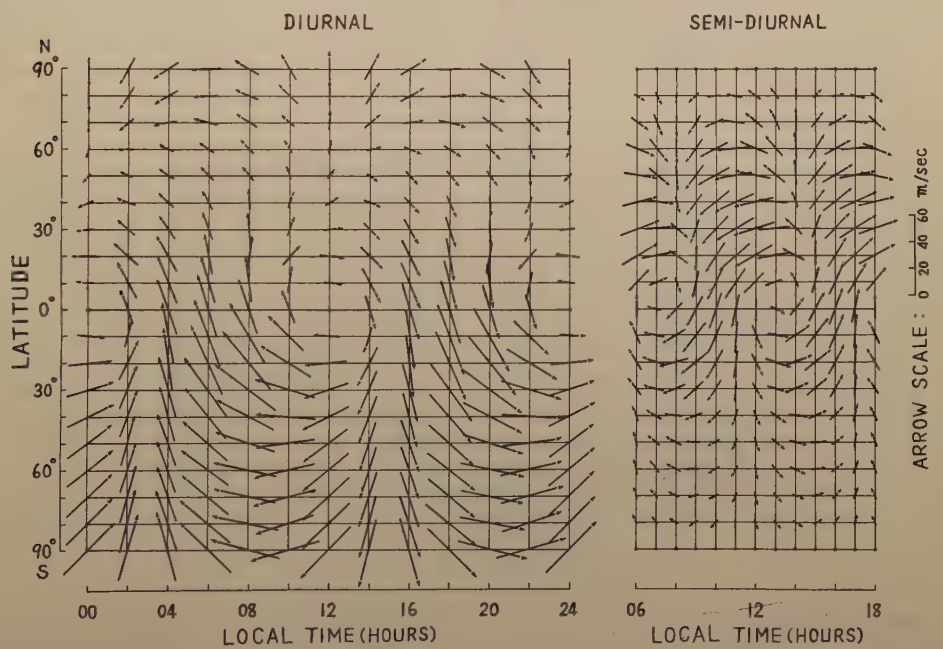

Fig. 5 Distributions of the wind velocity in Northern winter for each of the diurnal (left) and semi-diurnal (right) components.

for both hemispheres.

(*b*) *Semi-diurnal wind component*

1) The 12-hourly harmonics represent a clockwise rotation in the Northern hemisphere, and an anticlockwise rotation in the Southern hemisphere. 2) The movement is towards the North (South) at 1130 and 2330 hr in summer in the Northern (Southern) hemisphere, and at 0230 and 1430 hr in winter in the Northern (Southern) hemisphere. 3) The magnitude of the rotating vectors is about 10 m/sec in summer, and about 20 m/sec in winter, for both hemispheres.

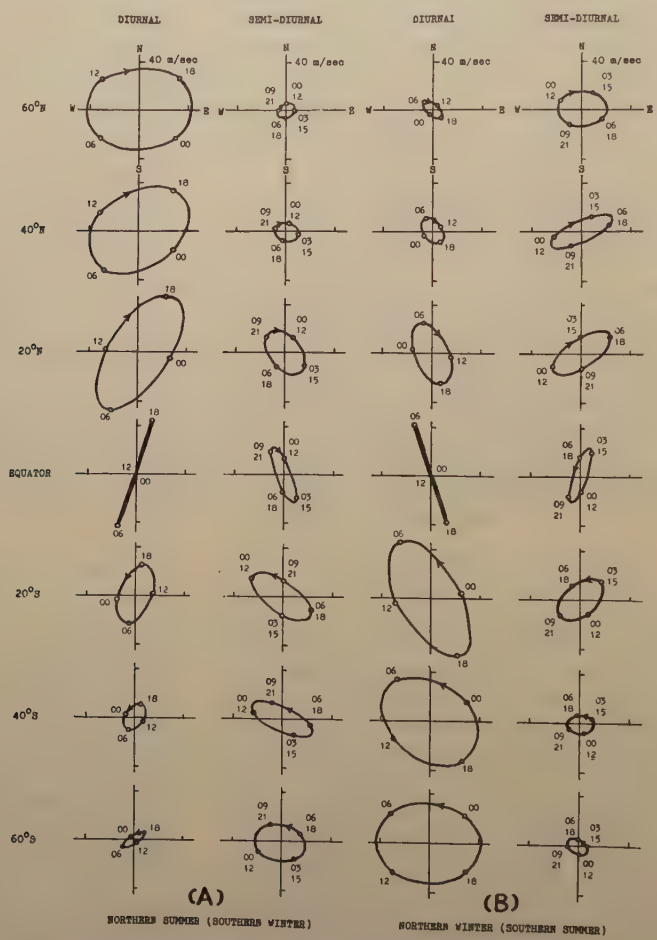

Fig. 6 Polar plots of the diurnal and semi-diurnal wind components at latitudes of 0°, 20°N and S, 40°N and S, and 60°N and S, in Northern summer (A) and in Northern winter (B).

5. Summary and Discussion

The wind systems required to produce the geomagnetic S_q variations in Northern summer and winter are deduced from the dynamo theory. The wind vector associated with both harmonic components rotates clockwise in the Northern hemisphere, and anti-

clockwise in the Southern hemisphere. This direction of the rotation and the magnitude of the rotating vectors are in general agreement with the observed results [8] (for both harmonics) [9, 10] (for semi-diurnal). However, the phase of the rotation does not agree with the observed one. The observed phase is such that the diurnal wind component blows towards the South near 0600 hr in the Southern hemisphere [8], and that the semi-diurnal wind component blows towards the North (South) near 0600 and 1800 hr in the Northern (Southern) hemisphere [8, 10]. The difference between the calculated and observed phases may be accounted for by the fact that the winds at altitudes of 80–100 km which are probably lower than the dynamo region are measured by the radio-echo meteor technique.

The diurnal wind vectors have greater magnitude in summer than in winter, whereas the semi-diurnal wind vectors have smaller magnitude in summer than in winter over most of the hemisphere. And, in summer hemisphere the diurnal component of winds is greater than the semi-diurnal one, whereas in winter hemisphere the former is more or less smaller than the latter. This situation seems to be consistent with the results observed by L. Harang and K. Pedersen [11]. For the sake of exact comparison, however, further systematic measurements of ionospheric winds, especially in the dynamo region (100–130 km), are still necessary.

6. Acknowledgments

The author wishes to express his sincere thanks to Prof. M. Hasegawa and Prof. K. Maeda for their valuable discussions and advice, and to Prof. Y. Tamura and Dr. M. Ota for their continued interest and support in the course of this study. He is also very grateful to Mr. A. Kijima who had kindly taken the trouble to check our solution of the differential equations by Integro-Differential Analyser.

References

[1] H. Maeda, J. Geomag. Geoelectr., **7**, 121 (1955).
[2] S. Kato, J. Geomag. Geoelectr., 8, 24 (1956).
[3] M. Hirono and T. Kitamura, J. Geomag. Geoelectr., 8, 9 (1956).
[4] S. Kato, J. Geomag. Geoelectr., **9**, 107 (1957).
[5] H. Maeda, J. Geomag. Geoelectr., **5**, 39 (1953).
[6] M. Hasegawa and M. Ota, Read at the Meeting of the Japanese Society of Terrestrial Magnetism and Electricity, Oct. 16, 1956.
[7] H. Maeda, Rep. Ionosph. Res. Japan, **10**, 49 (1956).
[8] W. G. Elford and D. S. Robertson, J. Atmosph. Terr. Phys., **4**, 271 (1953).
[9] B. H. Briggs and M. Spencer, Phys. Soc. Rep. Prog. Phys., **17**, 245 (1954).
[10] J. S. Greenhow and E. L. Neufeld, Phil. Mag., **46**, 549 (1955).
[11] L. Harang and K. Pedersen, J. Geophys. Res., **62**, 183 (1957).

Disturbances in the Ionospheric $F2$ Region Associated with Geomagnetic Storms III. Auroral Latitudes

By Teruo SATO

Geophysical Institute, Kyoto University

(Read, Oct. 10, 1957; Received, Oct. 20, 1957)

Abstract

A study is made, based on the electron drift theory, of ionospheric $F2$ disturbances in the auroal latitudes associated with geomagnetic storms. The process of the study is analogous to that in middle and lower latitudes as shown in the previous papers I and II. The results show that $F2$ disturbances in the auroral latitudes, as well as those in lower ones, are ascribed to the effect of the vertical drift of the electron caused by electric field deduced from the geomagnetic disturbance-daily variation.

1. Introduction

Ionospheric $F2$ disturbances in the auroral latitudes associated with the geomagnetic storm have not yet been fully studied statistically. One of the reasons is that on a magnetically disturbed day a full observation on the $F2$ region is impossible owing to absorption of the radio wave or an obscuration due to the sporadic E region, hence the disturbance variations of the f_0F2 and h_pF2 (critical frequency and the height of the maximum electron density of the $F2$ region) are difficult to obtain. In spite of these circumstances, some results for variation of the f_0F2 are obtained by Nagata [1], Martyn [2] for an average state and by Meek [3], Obayashi [4] for individual ones. A variation of the $h'F2$ (virtual height) is obtained by Martyn [2], but, the result seems to be doubtful, since retardation of the radio wave was not taken into cosideration. On the other hand, theoretical studies have been made by Nagata [1] Meek [5] (thermal expansion theory) and Martyn [2], [6], Maeda [7] (ionization drift theory). But their treatments are confined mainly to supposition or rough estimations of the order of variation, and detailed calculations have not yet been made.

We have shown in two previous papers [8], [9] (hereinafter referred to as I and II) with the same title as the present that the $F2$ disturbances in the latitudes below the auroral can be well explained as an effect of the vertical drift of the electron due to the electric field deduced from the disturbance-daily (Ds) variation of the geomagnetic field. In this paper we further attempt to explain the auroral $F2$ disturbances as the same effect. For this purpose a statistical study is made in detail of deviated variations of f_0F2 (Δf_0F2) and h_pF2 (Δh_pF2).

2. Statistical Results of the Auroral $F2$ Disturbances

The ionospheric data used here are those at Tromsö (geographic lat. 69.4, geomagne-

tic lat. 67.1) Mar. 1956-Feb. 1957 and Jan.-Dec. 1952 and those at College (geograph. lat. 64.9, geomag. lat. 64.5) Mar. 1956-Feb. 1957 and Jul. 1941-Jun. 1946. As will be mentioned below, the variation of the f_0F2 is greater and more conspicuous in the period of larger sunspot number. Therefore it seems to be appropriate to use the data during the years 1956-1957 in order to know the average daily variations of the Δf_0F2 and Δh_pF2 in two stations.

(a) Daily variations of Δf_0F2 and Δh_pF2 and the seasonal change

(i) Daily variation of Δf_0F2

The daily variations of the Δf_0F2 in three seasons are shown in Fig. 1 (a), (b) by the dotted line. It is clear from these figures that most remarkable feature of the variation is maximum depression of the f_0F2 near noon in winter and equinox (sometimes second maximum near 18h) and a depression throughout a day in summer. The hours of the negative Δf_0F2 in a day become larger in summer than in equinox and in equinox than in winter, while the hours of the positive Δf_0F2 become shorter.

We consider that these phenomena depend on the hours of the sunshine of a day and on the height distribution of the decay coefficient (see **4** and **5**).

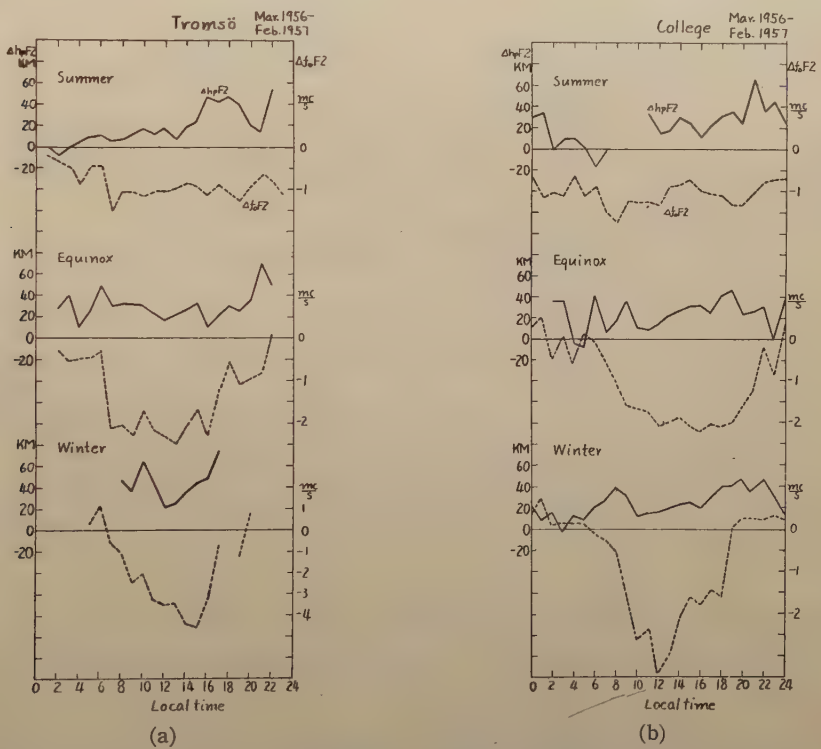

Fig. 1 (a) (b) Mean daily variations of Δf_0F2 (dotted line, right ordinate) and Δh_pF2 (full line, left ordinate) in three seasons.

(ii) Daily variation of Δh_pF2

For the deviation of the h_pF2, it must be noted that the effect of the retardation of the radio wave by the $F1$ region is in some cases included in the h_pF2. That is to

say, as the value of the f_0F2 approaches that of the f_0F1 owing to geomagnetic storm effect, the $h'F2$ becomes larger and larger. This is case also for the h_pF2, because the h_pF2 is calculated by mathematical treatment for one parabolic region. In order to remove this retardation effect we use the same method as in the paper II.

Process of removal of the retardation effect is applied mainly to the data in summer and partially those in equinox, whence the f_0F2 on the quiet day is comparatively low. In these seasons, the retardation effect is also included in the h_pF2 on the quiet day, so that we must use, as a median value, the h_pF2 freed from this effect, obtained by the process which is the same as that on the disturbed day.

The daily variation of the h_pF2 obtained after the above reatment is shown in Fig. 1 (a), (b) by full line. The main feature of the variation is to have two maximums of the positive value (increment) of the h_pF2 near 6–8h and near 16–18h. The interval of these two maximums depends on the season and is largest in summer and shortest in winter. As shown in the latter section, earlier maximum of a day seems to occur by the superposition of the upward motion of the electron mass and the electron production at and after sunrise and the latter maximum by a direction change of the electron mass from upwards to downwards. For comparison the daily variations of the Δf_0F2 and $\Delta h'F2$ in lower latitudes are shown in Fig. 2.

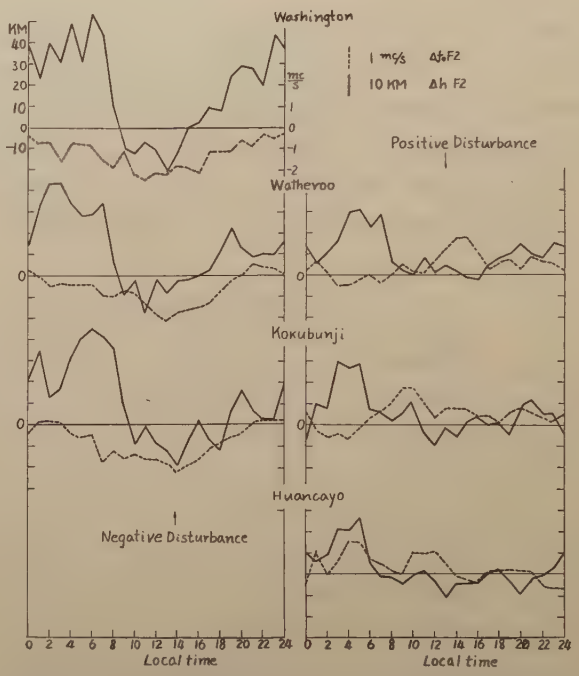

Fig. 2 Mean daily variations of Δf_0F2 (dotted line, right ordinate) and $\Delta h'F2$ (full line, left ordinate) in four stations in middle and low latitudes for two types of disturbances. Data ; 1949–1956 for Washington and Kokubunji, 1938-1944 for Wathero and Huancayo. (after Sato [9])

(b) **Relations between Δf_0F2 and geomagnetic activity, sunspot number**

Since the magnitude of the Δf_0F2 is considered to depend on both geomagnetic activity and sunspot number (in other words, f_0F2, which is proportional to the number), it is better to put in statistics under a certain activity or number. Similar statistics made in II for Washington and other stations are insufficient, because the above consideration has not been taken. Fig. 3 (a), (b) and Fig. 4 (a), (b) show the mean values $(\overline{\Delta f_0F2})$ of the Δf_0F2 during three hours centered on noon. In the former figure the values of the $\overline{\Delta f_0F2}$, in 1942 (near the minimun sunspot number) and in 1956 (near the maximum one), are shown against the value of ΣK_p (a day sum of K_p indices) and in the latter

the value of the $\overline{\Delta f_0F2}$ is shown against the Zurich provisional sunspot number with a different sign for different geomagnetic activities. From these figures it is clear that

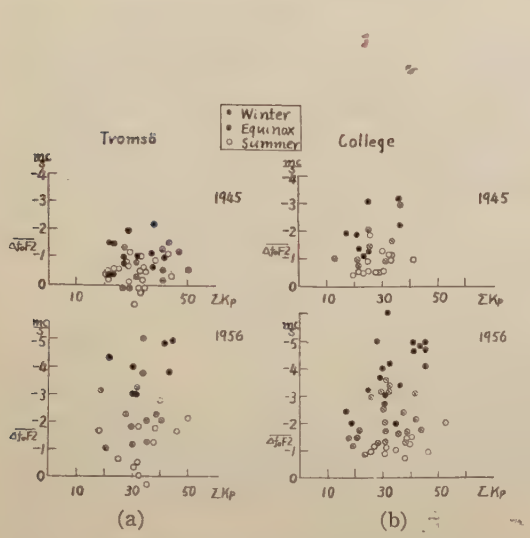

Fig. 3 Relation between $\overline{\Delta f_0F2}$ (mean value of Δf_0F2 during three hours centered on noon) and ΣK_p (a day sum of K_p indices) in 1945 (year near minimum sunspot number) and in 1956 (year near maximum one)

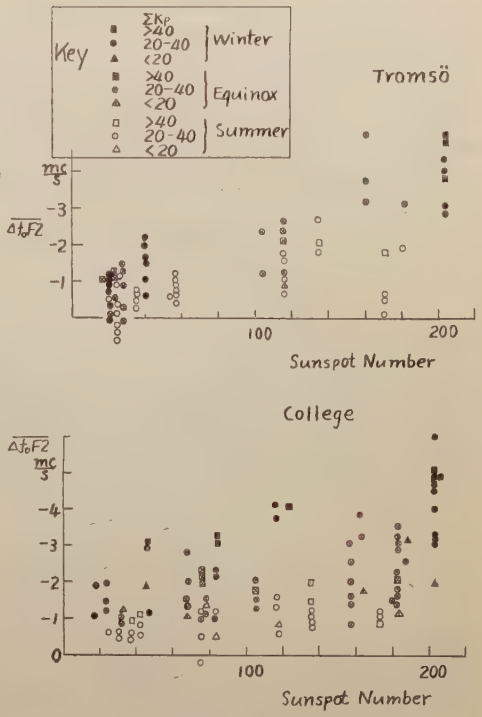

Fig. 4 (a), (b) Relation between $\overline{\Delta f_0F2}$ and sunspot number

(i) the negative value of $\overline{\Delta f_0F2}$ increases with the increasing ΣK_p in each season,

(ii) the negative value of $\overline{\Delta f_0F2}$ increases with the increasing sunspot number in each season, and

(iii) the negative value of $\overline{\Delta f_0F2}$ is largest in winter and smallest in summer.

From (ii) and (iii) it seems that severer disturbances occur in winter than in other seasons and in a year of a greater sunspot number. But the above assertion is not true, because the percentage of decrease of the electron density seems to be about the same, regardless of the season and the sunspot cycle. For example, the maximum decrease of the f_0F2 at sunspot number near 200, 120 and 40 in winter at College is about 5 mc/s, 4 mc/s and 3 mc/s respectively, whereas the median values of the f_0F2 at noon on the quiet day for the corresponding numbers are 11 mc/s, 8 mc/s and 6 mc/s. Hence the rates of the decrease are about the same. Similar situations hold for the rates among the seasons. Therefore the phenomena (ii) and (iii) are ascribed to a fact that the f_0F2 at noon in winter (especially, Nov., Feb.) is greatest in winter and smallest in summer and that the f_0F2 increases linearly with the increasing sunspot number. In a year of very small sunspot number, the f_0F2 is small and approaches the f_0F1, hence the decrease of the f_0F2 on the disturbed day seems apparently to be small, for the decrease below the f_0F1 is not known. The phenomenon (i) is considered to be

an increase of the vertical drift velocity (see **4, 5**).

3. Theoretical Considerations

We assume that the vertical drift of an electron on the disturbed day is caused by an electric field deduced from the geomagnetic Ds variation. When an anisotropic electrical conductivity is taken into account and the winds in the F and E regions are assumed to have the same directions and magnitudes, the electric current, I_x and I_y, in the directions x (south) and y (east) are given by

$$\begin{aligned} I_x &= k_x E_x + k_{xy} E_y, \\ I_y &= k_{yx} E_x + k_y E_y, \end{aligned} \tag{1}$$

where

$$k_x = \int_E \sigma_{xx}\, dz + \int_F \sigma_{xx}\, dz, \quad \text{etc.} \tag{2}$$

and σ_{xx} etc. are the elements of the electrical conductivity tensor $\{\sigma\} = \begin{Bmatrix} \sigma_{xx} & \sigma_{xy} \\ \sigma_{yx} & \sigma_{yy} \end{Bmatrix}$ (we use this notation instead of $\{\sigma'\}$ in I and II). The integration in (4) is carried out throughout the F and E regions. E_x and E_y are the electric fields in the x and y directions. From (1) we obtain

$$E_y = \frac{I_x}{K_{xy}} + \frac{I_y}{K_y}, \tag{3}$$

where

$$K_{xy} = \frac{\Delta}{k_{xy}}, \quad K_y = \frac{\Delta}{k_x}, \quad \Delta = k_{xy}^2 + k_x k_y. \tag{4}$$

I_x and I_y are approximately related to the geomagnetic components in y and x directions, ΔY and ΔX, in such a way that

$$\begin{aligned} 2\pi I_x &= f \Delta Y, \\ 2\pi I_y &= -f \Delta X, \end{aligned} \tag{5}$$

where f is a constant and taken as unity. Then the vertical drift velocity is given by

$$v = \frac{E_y}{F}\cos\phi = \left(\frac{I_x}{K_{xy}} + \frac{I_y}{K_y}\right)\frac{\cos\phi}{F}, \tag{6}$$

where F is total intensity of geomagnetic field at the station and ϕ is the geomagnetic dip. If ΔX and ΔY are the values deduced from the Ds variation and K_{xy} and K_y are the values on a disturbed day, the value v equals to the velocity v_d on the disturbed day. In the course of the study it is nesessary to know the daily variations of the $F2$ region on a quiet day. The vertical drift of the electron on a quiet day is considered to affect the quiet daily variation of the $F2$ region. The vertical velocity of the electron (v_q) on a quiet day is obtained by the same expression as (6), replacing the electrical conducitivity and the variations of the geomagnetic field in the expression by the values on the quiet day. In this case the values of ΔX and ΔY are those derived from the mean value of the S_q variations of five international quiet days in the month when a storm occurs.

If the effect of the horizontal velocity and the hight gradient of the vertical velocity

are not taken into account, the variation of the electron density is given by

$$\frac{\partial n}{\partial t}=q(z,t)-\beta(z)n-v(t)\frac{\partial n}{\partial z} \qquad (7)$$

where n represents the electron density, v the vertical velocity of the electron, q and β the production and the effective attachment rates of the electron respectively, t the time and z the height in unit of the scale height. q is taken as $q_0\,exp\,(1-z-e^{-z}sec\chi)$, where q_0 is a constant and χ is the solar zenith angle. The equation (7) is solved by the numerical method firstly attempted by Milllngton [10]. Then the equation is replaced by the following forms

$$\sigma_0\frac{d\nu}{d\phi}=|F|_z-|\xi|_z\nu, \qquad \frac{dz}{d\phi}=1.37\times10^4v \qquad (8)$$

where $t=1.37\times10^4\phi$, $1/\sigma_0=1.37\times10^4\beta_0$, $1/n_0=\beta_0/q_0$, $\nu=n/n_0$, $\beta=\beta_0|\xi|_z$ (β_0 is constant). If the velocity v equals to v_q the solution of the equation represents the daily variation on a quiet day and if v equals to (v_q+v_d) the solution represents that on a disturbed day. When the former variation is subtracted from the latter the residuum equals to the deviation from the normal variation.

4. Observed and Calculated Results for Individual *F*2 Disturbances

In this section we study whether the individual state of the $F2$ disturbance can be accounted for as an effect of the vertical drift of the electron. For the deduction of the drift velocity on a disturbed day the following points are taken into consideration. At first, in order to obtain the necessary Ds variation from one geomagnetic storm the convenient method as shown in II is adopted. That is, the values of the horizontal intensity (H) and the declination (D) of the geomagnetic field for the local time nearest to that of the commencement of a geomagnetic storm, are taken, and from these values mean values of H and D on the five international quiet days corresponding to that hour, are respectively subtracted. The values thus obtained are the deviative parts at zero hour of the storm time. The process is followed for the succeeding 60 hours. They are denoted as ΔH and ΔD. Next the overlapped mean of 24 hours of them are calculated for the former 48 hours, assuming that the deviative values befor the commencement of the storm are zero. Then the variations can be said to correspond to Dst variation of an average state. When these variations are subtracted respectively from ΔH and ΔD, the parts corresponding to the Ds variation of an average state can be derived.

Secondly we must estimate the magnitudes of the conductivity K_{xy} and K_y. It is probable that the electrical conductivity of the ionosphere increases on a disturbed day in the auroral latitudes, owing to an increase of the ionization by the particle or other ionizing agencies [11], [12]. However, the height-integrated conductivity depends on the height interval and also an estimated height of the maximum electrical conductivity of the ionosphere seems to lie at or above the E region [13], [14], [15], [16]. So that it is unlikely that the height-integrated electrical conductivity of the ionosphere increases

on the disturbed day far greater than that on the quiet day, even if the electron density increases so much in the E or below the E region. Hence we assume that K_{xy} and K_y are respectively twice the noon values of them on the quiet day (daily variation is the same as in Table 1 in II) and they are constant throughout a day. Then

$$K_{xy}=\begin{cases}8.0\times10^{-8}\text{ e.m.u., summer}\\ 7.2\times10^{-8}\text{ e.m.u., equinox.}\end{cases}\quad K_y=\begin{cases}6.4\times10^{-8}\text{ e.m.u., summer}\\ 5.8\times10^{-8}\text{ e.m.u., equinox.}\end{cases}\qquad(9)$$

For the calculation of the deviative part, the important point to pay an attention is the height distribution of the attachment coefficient β. In I and II the distribution A in Fig. 5 is used and results of the calculations show that this distribution is fairly correct. However, the fact that as the night lengthens (as the season approaches winter), the durations and magnitude of the positive values of the Δf_0F2 and Δh_pF2 increases remarkably shows that the above distribution A is not satisfactory, because the use of A does not bring the large positive value of the Δf_0F2. The above statistical results show that the rate β decreases with increasing height; for example, a distribution B (further discussions will be stated in the section **7**, ii). In the present caulculations two distributions are used and the results compared.

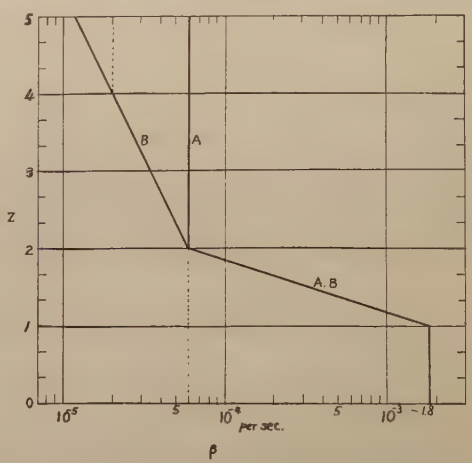

Fig. 5 Height distribution of β. Height 0 corresponds to the height of Chapman's maximum production.

The individual $F2$ disturbance (Δf_0F2 and Δh_pF2) and the corresponding calculated variations (deviation of the electron density and Δh_pF2) are shown in Fig. 6. The data in the examples are those at Tromsö, 1952, as the ionospheric data in a large sunspot number year which we have at hand are not accompanied by the geomagnetic data. (we have no geomagnetic data at College). The ionospheric data on the disturbed day want a record much frequently, the examples are limited to some disturbances which have comparatively a lot of record. Now in Fig. 6 (A) represents observed results and (B), (C) corresponding calculated variations using the distribution of β, respectively A, B and (D) the Ds variations of the ΔH and ΔD. From these figures it is found that the calculated results are well consistent with the observations. Generally the caulculated positive variation of the Δh_pF2 is larger and continues longer for the distribution B than A and inversely the calculated negative deviation of the electron density is smaller. In the example (d) in Fig. 6 where the disturbance in September is shown, the increase of the electron density at night is seen when the distribution B is used. In this example the positive value of the Δf_0F2 is not shown. But, as statistical results show a remarkable increase of the Δf_0F2 in this season, it is clear that the distribution of β such as B is needed.

5. Observed and Calculated Results for Average State of $F2$ Disturbances

Since in an individual disturbance the record is few, it is difficult to compare fully calculated results with observation. In order to remove this defect, the variation of an average state and the corresponding calculated variation are compared. For this purpose, usually, a lot of calculated variations for individual state are put in statistics and the results compared with the corresponding statistical results of the observed data. But this method is much laborious and besides, the method of the derivation of the *Ds* part of the geomagnetic field, is of approximate. Therefore another process is adoped here. At first ΔH and ΔD are obtained for many storms, they are arranged according to the storm time and the mean of them respectively calculated. These mean values are subtracted from ΔH and ΔD and the residuum are rearranged according to the local time. Then the means of them represent the *Ds* variations. Using these *Ds* variations and the same electrical conductivity as that in the previous section we can obtain a mean vertical velocity of the electron drift. Then calculated deviations during 48 hours are obtained for the moving mass with the above velocity but with a different begining time. They are arranged according to the local time and the mean of them can be regarded as an average state. For the sake of simplicity, the representative beginning time is taken as 0, 6, 12 and 18 h of the local time. The data used for the calculations are those at Tromsö, 1952. The calculations are made for an average state

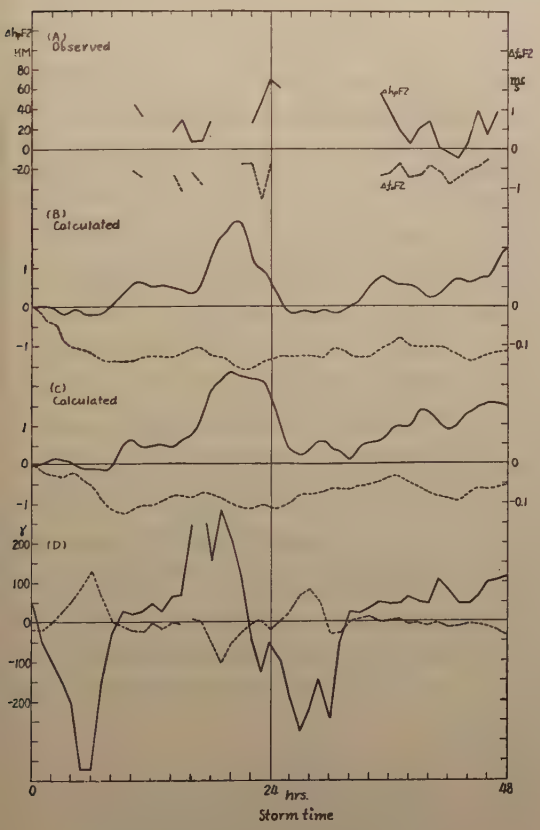

(a) Tromsö, 20 h, Aug. 9., 1952

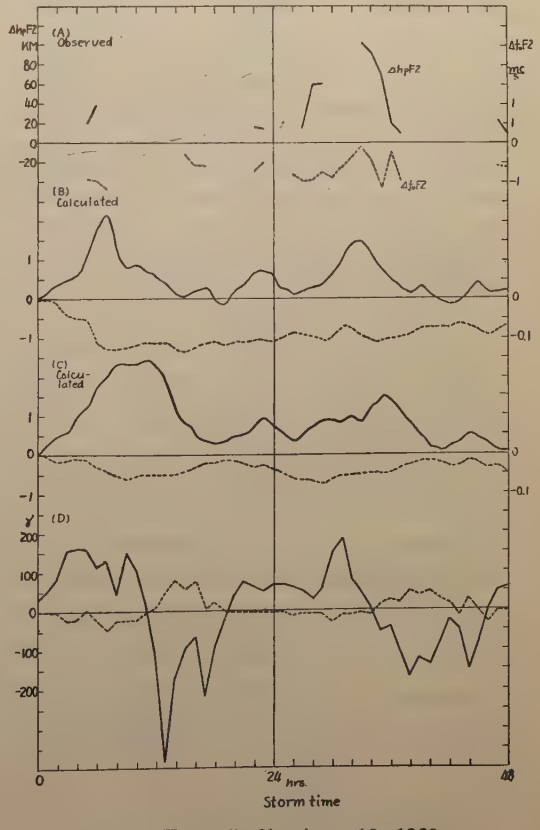

(b) Tromsö, 9h, Aug. 18, 1962

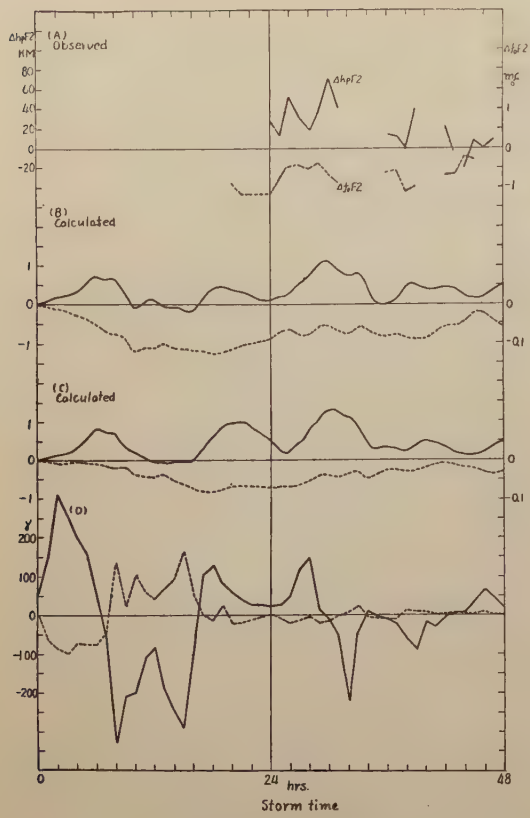

(c) Tromsö, 13h, Aug. 29, 1952

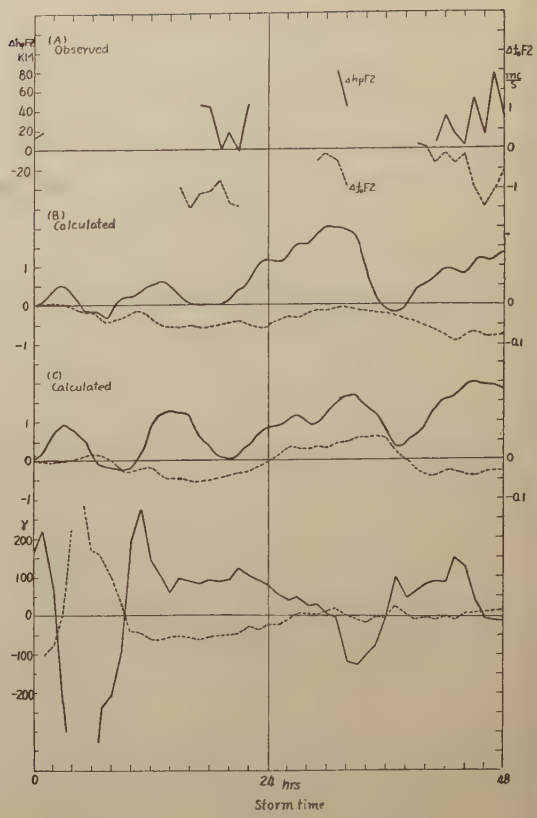

(d) Tromsö, 20h, Sep. 25, 1952

Fig. 6 (a)–(d) (A) represents the observed variations of Δf_0F2 (dotted line, right ordinate) and Δh_pF2 (full line, left ordinate) for the $F2$ disturbance which begins at the time shown below. The time is the nearest local time before the beginning of the geomagnetic storm and this is taken as zero of the storm time. (B) represents the calculated variation of the deviation of the maximum electron density* (dotted line, right ordinate) and the height (full line) using the distaibution A in Fig. 5, (C) the calculated variation of them using the distribution B and (D) the observed variations of ΔH (full line, left ordinate) and ΔD (dotted line, in γ, left ordinate).

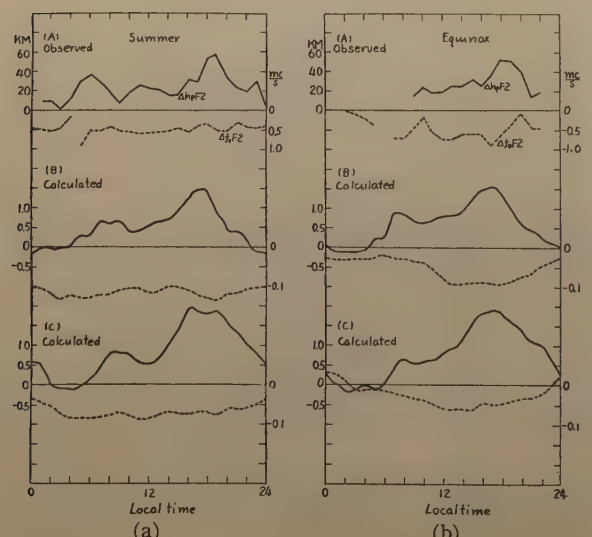

Fig.7 (a), (b) (A) represents the observed mean daily variations of Δf_0F2 (dotted line, right oridinate) and Δh_pF2 (full, line) in summer and equinox at Tromsö, 1952, (B) the calculated variations of the maximum electron density* (dotted line, right ordinate) and the height (full line) using the distribution A in Fig. 5 and (C) the calculated variations for them using the distribution B.

* Note that the day maximum of the maximum electron density on the quiet day lies between 0.2 and 0.3 (dimensionless) for summer and equinox.

in equinox and summer and not for that in winter. The reason is the following. If the ionization in the $F2$ region is caused by sun's radiation as shown by Chapman, the ionization in high latitudes such as auroral or polar is to be zero in December. Nevertheless the electron density is fairly large in these latitudes. This seems to show that production or penetration of the electron by any other mechanisms becomes effective in winter in these latitudes, and their mechanisms are not yet revealed.

Average states and the corresponding calculated variations are shown in Fig. 7. (a), (b). In these figures (A) to (C) correspond to those in Fig. 6. Observed results are well analogous to those in Fig. 1 and the calculated variations are consistent with observed ones. It is noted that an increase of the electron density at night is shown in equinox when the distribution B is used, but judging from the magnitudes of the variations it appears that the necessary distribution of β is an intermediate one between A and B but closer to A.

6. Physical Interpretation of Disturbance Variation

Based on the above calculations, we state physically as for the deviations of the f_0F2 and h_pF2 in the disturbance. The vertical velocity of the drift deduced from the geomagnetic Ds variation is upwards about from 6h to 18h and downwards from 18h to 6h, regardless of the season. In the absence of the electron production the upward motion of the electron mass with the maximum density shows a deviation in height which equals to the time-integration of the velocity, but if the production begins at sunrise the height of the maximum density rises abruptly, owing to the production of an ionization layer at great height with a larger density than the maximum one of the electron mass which already existed before sunrise. Soon after an accumulation of the electron sets up below the height of the second maximum, the maximum density to be measured moves down to the third maximum. As an electron mass of the third maximum density still moves upwards, a fourth maximum density sets up below the height of the third, and so on. When sunset approaches an accumulation of the electron in the lower region becomes small, the upward drift becomes effective and the height of the maximum again increases remarkably. Thus the height of a maximum density does not so much move upwards in strong radiation of the sun (near noon), except a large drift velocity, and begins to move upwards, till a downward motion begins, when the sun's radiation becomes weak. Therefore it is easily recognized that an interval between two maximums of increase in the h_pF2 is shorter in winter than in other seasons. In a downward motion of an electron mass with the maximum density, the height of the maximum falls downwards, and finally, the height remains stationary at a level where an abrupt increase of the electron decay begins. This is because the maximum electron density in the region of a large decay coefficient decreases more rapidly compared with a decay in higher regions.

On the other hand, the maximum electron density on the sunlit time (upward drift in winter and equinox) becomes smaller than the median value, because an accumulation is difficult to take place due to the movement. The decrease of density is amplified by

an increase of the drift velocity. In summer when the sun is present throughout a day the electron density decreases compared with the median value, because of the penetration of the electron mass to the region of the large decay coeficient (18h–6h), as well as, of the difficulty of the electron accumulation. This circumstance does not vary when the distribution B of β is used. In winter the situation during the sunlit time is the same as that in summer, however the production is shut out on the way of the upward motion and the maximum electron density lying at the higher altitude than the median height decreases much less than the decrease of the median maximum density owing to the smaller decay coefficient, when the distribution B is used. So that an observed value on a disturbed day increases more than that on a quiet day. The increase continues until the density subjects to a rapid decay in the lower region due to a downward motion or the sun's radiation begins to produce an ionization. Thus the larger the hours of the night, the larger the increase of the electron density.

7. Discussions

(i) It is considered that on a quiet day the height-integrated electrical conductivity in the auroral latitudes is the same order of magnitude as that in middle latitudes, inferring from the geomagnetic S_q variation in those latitudes and that on a disturbed day the electrical conductivity on the former latitudes increases whereas that on the latter does not vary. In the present calculations we assume the ratio of increase of the electrical conductivity in the auroral latitudes to be 2. This order of magnitude of the increase seems to be slightly small, compared with the values assumed by other authors. For example, the ratio is taken as 10 by Maeda [7] 10 by Fukushima and Oguchi [7], 3–30 by Matsushita [18] and 100 by Jacobs and Obayashi [19]. A high ratio is necessary to obtain enough intensity of the current to explain the observed results in the dynamo theory of the S_D current system. But if the $F2$ disturbance in the auroral latitudes is ascribed to the effect of an electron drift as shown in this paper, the ratio should be in a range of 2–4 and cannot be any higher value, since otherwise the drift velocity on a disturbed day becomes far smaller than that on a quiet day, and the effect of the former drift becomes negligible.

It may be considered that an ionization in the aurora is fairly large and contribute to an increase of the electical conductivity. Indeed, the electron density shown by Curie *et al* [20] and Bullough and Kaiser [21] respectively is very large, but as shown by Omholt [22] the electron density in the aurora appears to be about $(2\text{–}10)\times 10^5$/cc and high values by Currie and others may be the ones occurred partially or temporarily. A sporadic slant E and a blackout in the auroral latitudes are associated strongly with the geomagnetic bay or the bay-type variation during a storm [5] [12] and these phenomena imply an increase of the ionization. Thus the electron density may increase by a few times or there about. But the level seems to lie below the level of the maximum electrical conductivity and the height range is probably small, hence it cannot be said that the height-integrated value increases with the same rate.

Martyn states that the polarization field sets up originally in the auroral latitudes,

spreads over the earth and the current system due to this field has the strength and the form required to explain the main features of the geomagmetic S_D field. We do not then need to assume a different S_D wind system from the S_q and a great increase of the electrical conductivity necessary to explain the intensity in the dynamo theory of the S_D current system. Again, a strong electric field causes a drift of the electron and the $F2$ disurbance results which we show quantitatively in this paper.

(ii) The increase of the f_0F2 at night on a disturbed day may be derived by taking the height gradient of the vertical velocity of the electron into consideration. In this case it is necessary that the velocity increases upwards with a great gradient. But the drift velocity derived from the geomagnetic Ds variation is almost independent of the season and hence it seems to be difficult to account for the seasonal feature of the increase shown by the statistics. Furthermore if the velocity gradient is present in the auroral latitudes it must be present in middle latithdes, also. Then it becomes difficult to explain the negative disturbance in middle latitudes (similar to the disturbance in the auroral latitudes) since the phase of the drift velocity in middle latitudes is different by about 180°from that in the auroral latitudes.

The adoption of the distribution of β decreasing upwards shown in the secttion 4 removes the above inconsistency. This type of the distribution is analogous to the type suggested by Ratcliffe *et al* [23] and makes the calculated results for the disturbance in middle latitudes in II better.

We, however, do not at all abondon the presence of the height-gradient of the vertical velocity. On a disturbed day the gradient may be small for the large polarization field set up in the ionosphere, but on the quiet day the efiect of the gradient becomes remarkable. Anomalous quiet daily variation and the seasonal change of the electron density in the $F2$ region may be explained by considering the height gradient of the vertical velocity. Martyn [24] treats this problem under the night time condition, so that it remains to study the effect, including the electron production.

8. Conclusion

Our statistical results show that the deviation of the f_0F2 in the auroral latitudes on the disturbed day is similar to the negative disturbance in middle latitudes, while the deviation of the h_pF2 is different from above. The calculations of the effect of the vertical drift of the electron, show that the main features of the $F2$ disturbances in the auroral latitudes can be accounted for by this effect for an individual or average states.

We are now proceeding with the study of the $F2$ disturbances in the polar cap although the lack of the hourly values of the ionospheric and the geomagnetic observations make it finally difficult to go on with it.

Acknowledgement

The author wishes to express his hearty thanks to Prof. M. Hasegawa, Dr. M. Ota and Dr. M. Hirono of the Geophysical Institude, to Prof. K. Maeda of the Electronic

Engineering Institute, Kyoto University and to Prof. T. Nagata, and Dr. N. Fukushima of the Geophysical, Institute, Tokyo University for their kind advice and valuable discussions in the course of this study.

References

[1] T. Nagata, Res. Iono. Res. Japan, **8**, 39 (1954)
[2] D.F. Martyn, Nature, London, **171**, 14 (1953)
[3] J.H. Meek, J. Geophys. Res., **57**, 177 (1952)
[4] T. Obayashi, Rep. Iono. Res. Japan, **8**, 19 (1954); J. Geomag. Geoelectr., **6**, 57 (1954)
[5] J.H. Meek, J. Geophys. Res., **58**, 445 (1953)
[6] D.F. Martyn, Proc. Roy. Soc. Lon., A **218**, 1 (1953)
[7] K. Maeda, Rep. Iono. Res. Japan, **7**, 81 (1953)
[8] T. Sato, J. Geomag. Geoelectr., **8**, 129 (1956)
[9] T. Sato, J. Geomag. Geoelectr., **9**, 1 (1957)
[10] G. Millington, Proc. Phys. Soc., **44**, 580 (1932)
[11] S. Chapman and C.G. Little, J. Atmosph. Terr. Phys., **10**, 20 (1957)
[12] S. Matsushita, J. Geomag. Geoelectr., **8**, 156 (1956)
[13] K. Maeda, J. Geoelectr., **4**, 45 (1950)
[14] M. Hirono, J. Geomag. Geoelectr., **5**, 22 (1953)
[15] H. Maeda, J. Geomag. Geoelectr., **5**, 94 (1953)
[16] D.F. Martyn and W.G. Baker, Phil. Trans. **246**, 281 (1953)
[17] N. Fukushima and T. Oguchi, Rep. Iono. Res. Japan, **7**, 137 (1953)
[18] S. Matsushita, J, Geomag. Geoelectr., **5**, 109 (1953)
[19] J.A. Jacobs and T. Obayashi, Contract No. AF 19 (604)-761, Scientfic Rep. No. 4, University of Toronto.
[20] B.W. Currie, P.R. Forsyth and F.E. Vawter, J. Geophys. Res., **58**, 79 (1953)
[21] K. Bullough and T.R. Kaiser, J. Atmosph. Terr. Phys., **5**, 189 (1954)
[22] A. Omholt, J. Atmosph. Terr. Phys., **7**, 73 (1955)
[23] J.A. Ratcliffe, E.R. Schmerling, C.S.G. Setty and J.O. Thomas, Phil. Trans., *A* **248**, 621 (1956)
[24] D.F. Martyn, Proc. Roy. Soc., A **189**, 241 (1947)

Horizontal Wind Systems in the Ionospheric E region Deduced from the Dynamo Theory of the Geomagnetic S_q Variation Part IV

By Susumu KATO

Department of Electronics, Kyoto University

(Read, July 5, 1957; Received, July 10, 1957)

Abstract

Horizontal wind systems in the ionospheric E region are deduced along the same line as in a previous paper [1]. This time, however, the wind systems on both northern and southern hemispheres in the solstice season are obtained. The wind systems thus obtained represent the actual state instead of the mean state as in Part I and II [1] [3], in the solstice season. In Part IV the effect of the Coriolis force is taken into account and an advance is made in the treatment in Part III where the wind velocity is simply assumed to be irrotational [4].

It is shown, as in Part III, that in summer the diurnal wind motion is predominant over the semi-diurnal, whereas in winter the velocity of the former is almost the same as that of the latter. Further the diurnal wind velocity is greater in summer than in winter and the semi-diurnal wind velocity is somewhat smaller in summer than in winter.

Some differences are found between the results of Part III and IV. However, more observational material than available at present must be accumulated before discussing these differences,

1. Introduction

In Part I [3] H. Maeda deduced from the S_q variation the horizontal wind systems in the ionospheric E region in the mean solstice. Though the daily variability and the heterogeneity of the ionospheric conductivity were taken into consideration in his calculation, he simplified the treatment by neglecting the effect of the Coriolice force which plays an important role in the wind motion with such a long period as that of 24 or 12 hours. In Part II [1] the present author made an advanced treatment by taking the effect of the Coriolis force into account. His calculation was based on the same electric field in the ionosphere as that in Part I, but some differences were found between the results of Part I and II.

In both Part I and II the wind systems were deduced from the data of the S_q variation in the mean solstice, say $\frac{1}{2}(S+W)$, and the ionospheric conductivity in the equinox [3], and hence did not correspond to any actual case. Deduction of the wind systems on both hemispheres in the solstice season should be far significant for the purpose of direct comparison with the observational material.

In Part III and IV the wind systems on both hemispheres in the solstice season have been obtained. The northern and southern hemispheres correspond to the summer and winter respectively. In Part III (by H. Maeda) as in Part I a simple case was treated by neglecting the effect of the rotation of the earth. In this paper the effect of the rotation of the earth has been taken into consideration. The wind velocity is obtained by solving the dynamical equation of the atmosphere for the rotating earth simultaneously with the dynamo equation.

2. Differential Equation of the Dynamo Theory

The fundamental equations are

$$\boldsymbol{E}=\boldsymbol{v}\times\boldsymbol{H}+\boldsymbol{E}^{(S)}, \qquad \text{(e.m.u.)} \tag{1}$$

$$\frac{\partial \boldsymbol{v}}{\partial t}+2\boldsymbol{\omega}\times\boldsymbol{v}=-\operatorname{grad}\left(\frac{p'}{\rho_0}\right), \tag{2}$$

where $\boldsymbol{E}$ and $\boldsymbol{E}^{(S)}$ are the total and the static fields respectively, $\boldsymbol{v}$ the wind velocity, $\boldsymbol{\omega}$ the angular velocity of the earth and p' and ρ_0 the pressure variation and the static density of the ionosphere respectively. $\boldsymbol{H}$ is the magnetic field of the earth. As the static field has a potential,

$$\operatorname{curl}\boldsymbol{E}^{(S)}=0 \quad \text{or} \quad \boldsymbol{E}^{(S)}=-\operatorname{grad} S, \tag{3}$$

where S is a potential function. From (1) and (3) the wind velocity is given as follows;

$$\left.\begin{aligned} u&=-\frac{1}{H_z}\left(E_y+\frac{1}{a\sin\theta}\frac{\partial S}{\partial\lambda}\right),\\ v&=\frac{1}{H_z}\left(E_x+\frac{\partial S}{a\partial\theta}\right),\end{aligned}\right\} \tag{4}$$

where u, v are the southward and eastward components of $\boldsymbol{v}$ respectively, and E_x, E_y the southward and eastward components of $\boldsymbol{E}$ respectively. θ is colatitude and λ longiude. H_z is the vertically upward components of the geomagnetic field which is assumed to be $H_z=-C\cos\theta$ where $C=\frac{2}{3}\Gamma$. By taking the time factor as $e^{j\sigma t}$, operation of *curl* on (2) gives

$$j\sigma\left\{\frac{\partial u}{\partial\lambda}-\frac{\partial}{\partial\theta}(v\sin\theta)\right\}-2\omega\left\{\cos\theta\frac{\partial v}{\partial\lambda}+\frac{\partial}{\partial\theta}(u\sin\theta\cos\theta)\right\}=0. \tag{5}$$

Substitution of (4) into (5) yields

$$\begin{aligned}\frac{d^2S}{d\theta^2}+\frac{1}{\sin\theta\cos\theta}\frac{dS}{d\theta}-\frac{m^2}{\sin^2\theta}S=-a\Big[&\frac{dE_x}{d\theta}+\left(\frac{1}{\sin\theta\cos\theta}+2\cot\theta\right)E_x\\&+\frac{2j\cos\theta}{m}\left\{\frac{dE_y}{d\theta}+\left(\frac{m^2}{2\sin\theta\cos\theta}+\cot\theta\right)E_y\right\}\Big],\end{aligned} \tag{6}$$

where a is the radius of the earth.

In the above equation we put S, $\boldsymbol{E}\propto e^{jm\lambda}$ and $\sigma=m$ as in a previous paper [1]. The equation (6) is the differential equation governing the electro-static field. Substraction of the electro-static field from the total electric field gives the dynamo-induced field from which the wind velocity is readily obtained. If we put

$$E_x=\sum_m E_{x,m}=\sum_m\{a_m(\theta)\cos m(\omega t+\lambda)+b_m(\theta)\sin m(\omega t+\lambda)\},$$
$$E_y=\sum_m E_{y,m}=\sum_m\{c_m(\theta)\cos m(\omega t+\lambda)+d_m(\theta)\sin m(\omega t+\lambda)\},$$

and

$$S=a\sum_m S_m=\sum_m a\{A_m(\theta)\cos m(\omega t+\lambda)+B_m(\theta)\sin(\omega t+\lambda)\},$$

then (6) is divided into the following two equations.

$$\frac{d^2A_m}{d\theta^2}+\frac{1}{\sin\theta\cos\theta}\frac{dA_m}{d\theta}-\frac{m^2}{\sin^2\theta}A_m=f_m(\theta), \tag{7}$$

$$\frac{d^2B_m}{d\theta^2}+\frac{1}{\sin\theta\cos\theta}\frac{dB_m}{d\theta}-\frac{m^2}{\sin^2\theta}B_m=g_m(\theta), \tag{8}$$

where

$$f_m=-\left\{\frac{da_m}{d\theta}+\frac{1+2\cos^2\theta}{\sin\theta\cos\theta}a_m+\frac{2\cos\theta}{m}\left(\frac{dd_m}{d\theta}+\frac{m^2+2\cos^2\theta}{2\sin\theta\cos\theta}d_m\right)\right\},$$
$$g_m=-\left\{\frac{db_m}{d\theta}+\frac{1+2\cos^2\theta}{\sin\theta\cos\theta}d_m-\frac{2\cos\theta}{m}\left(\frac{dc_m}{d\theta}+\frac{m^2+2\cos^2\theta}{2\sin\theta\cos\theta}c_m\right)\right\}.$$

The right-hand side of (6), or f_m and g_m, is the function of the total electric field which was calculated from the data of S_q variations by H. Maeda [4].

3. Numerical method of integration

The differential equations (7) and (8) have regular singular points at $\theta=0$, $\frac{\pi}{2}$ and π. In order to obtain the analytic solution over the entire range of θ, some considerations should be given to A_m, B_m, $E_{x,m}$, and $E_{y,m}$ around these singular points.

1) around $\theta=0$

We expand the solution of (7) and (8), a_m, b_m, c_m, and d_m as a power series in θ about $\theta=0$:

$$\left.\begin{aligned}A_m&=A_{m,0}+A_{m,1}\theta+A_{m,2}\theta^2+\cdots\cdots\cdots,\\B_m&=B_{m,0}+B_{m,1}\theta+B_{m,2}\theta^2+\cdots\cdots\cdots,\end{aligned}\right\} \tag{9}$$

$$\left.\begin{aligned}a_m&=a_{m,0}+a_{m,1}\theta+a_{m,2}\theta^2+\cdots\cdots\cdots\cdots,\\b_m&=b_{m,0}+b_{m,1}\theta+b_{m,2}\theta^2+\cdots\cdots\cdots\cdots,\\c_m&=c_{m,0}+c_{m,1}\theta+c_{m,2}\theta^2+\cdots\cdots\cdots\cdots,\\d_m&=d_{m,0}+d_{m,1}\theta+d_{m,2}\theta^2+\cdots\cdots\cdots\cdots,\end{aligned}\right\} \quad m=1,2 \tag{10}$$

provided that the expansion is possible. In the above formulae, $A_{m,j}$, $B_{m,j}$, $a_{m,j}$, $b_{m,j}$, $c_{m,j}$, and $d_{m,j}$, are coefficients of expansion with θ^j. Since the eastward component of the static field is proportional to $\frac{S}{\sin\theta}$ and finite at $\theta=0$, then $A_{m,0}$ and $B_{m,0}$ must vanish. Further $a_{2,0}=b_{2,0}=c_{2,0}=d_{2,0}=0$ at $\theta=0$ according to the extrapolation of the geomagnetic data from the middle latitudes [3]. Substitution of (9) and (10) into (7) and (8) leads to

$$\left.\begin{aligned}3A_{1,2}&=\lim_{\theta\to0}[3\theta^{-1}(a_{1,0}+d_{1,0})+(4a_{1,1}+5d_{1,1})],\\3B_{1,2}&=\lim_{\theta\to0}[3\theta^{-1}(b_{1,0}-c_{1,0})+(4b_{1,1}-5d_{1,1})],\\\lim_{\theta\to0}3A_{2,1}\theta^{-1}&=-\lim_{\theta\to0}4(a_{2,1}+d_{2,1}),\\\lim_{\theta\to0}3B_{2,1}\theta^{-1}&=-\lim_{\theta\to0}4(b_{2,1}-c_{2,1}),\end{aligned}\right\} \tag{11}$$

In order that both sides of (11) are equal, the following conditions are given:

For $E_{x,1}$ and $E_{y,1}$

$$b_{1,0}=c_{1,0}, \qquad a_{1,0}=-d_{1,0}, \tag{12}$$

for $E_{x,2}$ and $E_{y,2}$

$$a_{2,1}=-d_{2,1}, \qquad b_{2,1}=c_{2,1}, \tag{13}$$

and for A_m, and B_m

$$\left.\begin{aligned} &A_{1,2}=\frac{1}{3}f_1(0)=\frac{1}{3}(4a_{1,1}+5d_{1,1}),\\ &B_{1,2}=\frac{1}{3}g_1(0)=\frac{1}{3}(4b_{1,1}-5c_{1,1}),\\ &A_{2,1}=0,\\ &B_{2,1}=0,\\ &A_{m,0}=B_{m,0}=0. \qquad m=1,2 \end{aligned}\right\} \tag{14}$$

together with

2) around $\theta=\frac{\pi}{2}$

We put $\theta'=\frac{\pi}{2}-\theta$ and expand A_m, B_m, a_m, b_m, c_m and d_m as in 1).

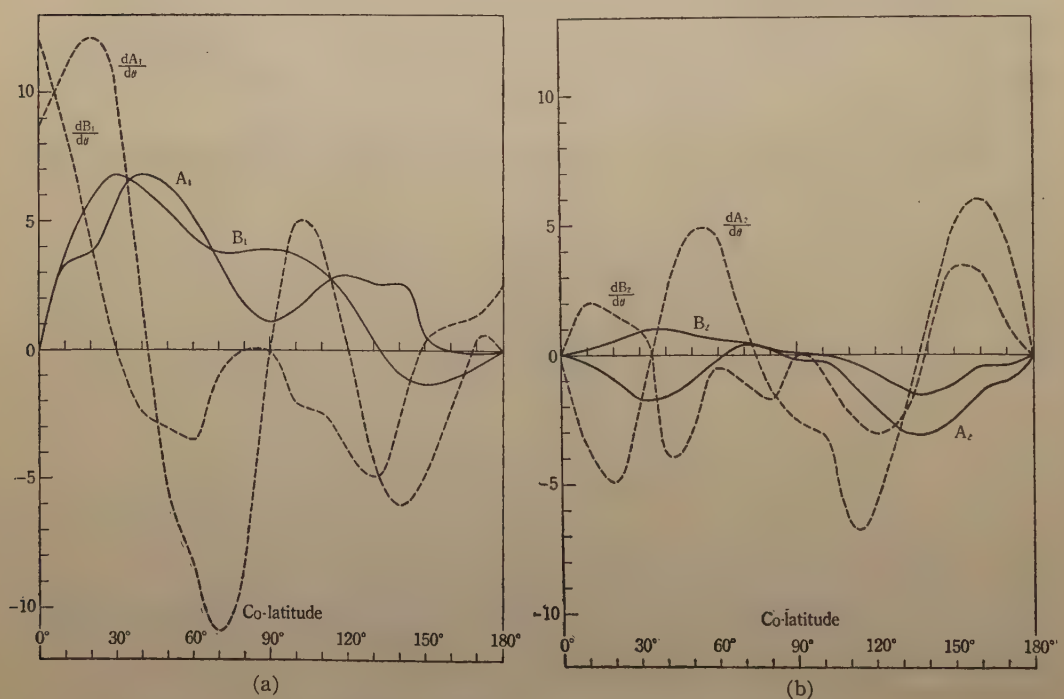

Fig. 1 A_m, B_m, $\frac{dA_m}{d\theta}$ and $\frac{dB_m}{d\theta}$ versus colatitude. Unit 10^2 e.m.u.

(a) $m=1$ The full line: A_1 and B_1. The broken line: $\frac{dA_1}{d\theta}$ and $\frac{dB_1}{d\theta}$.

(b) $m=2$ The full line: A_2 and B_2. The broken line: $\frac{dA_2}{d\theta}$ and $\frac{dB_2}{d\theta}$.

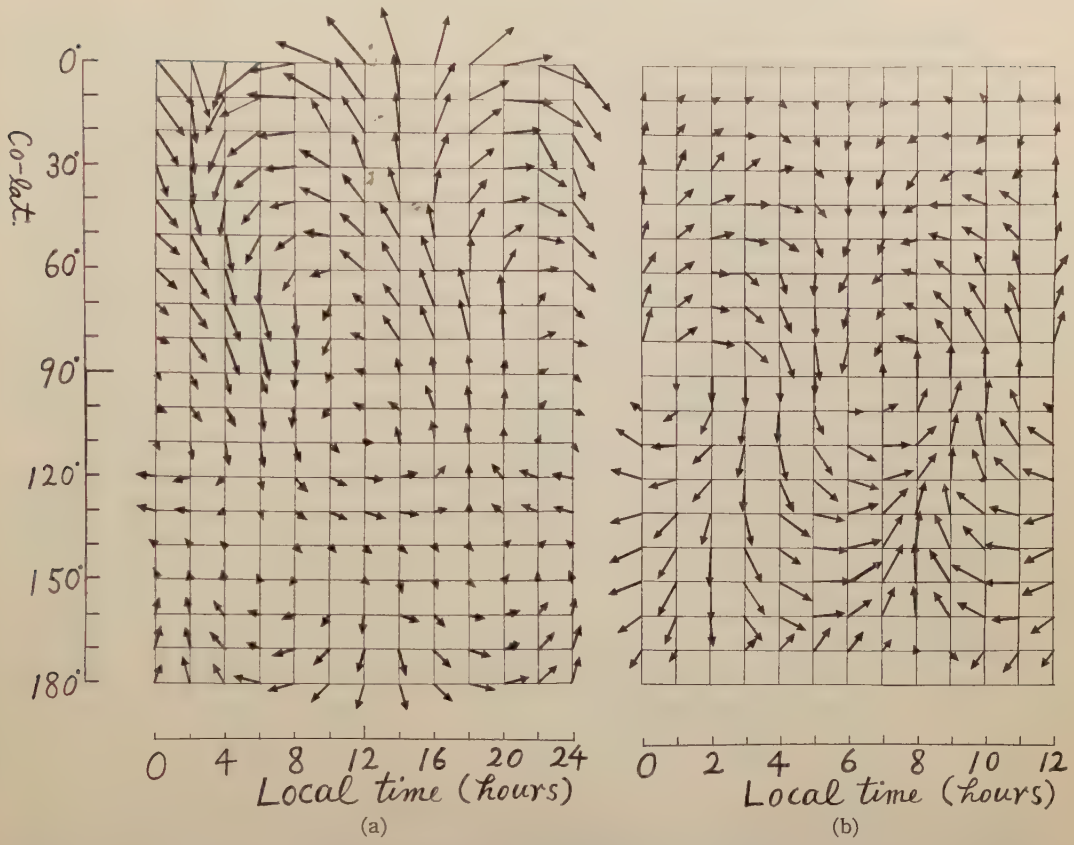

Fig. 2 Wind systems. Northern and southern hemispheres correspond to summer and winter respectively. (a) Diurnal component Arrow scale: 50 m/sec for a length equal to the side of the small squares. (b) Semi-diurnal component Arrow scale: 25 m/sec for a length equal to the side of the small squares.

Then

$$\left.\begin{aligned} A_m &= A'_{m,0} + A'_{m,1}\theta' + A'_{m,2}\theta'^2 + \cdots\cdots, \\ B_m &= B'_{m,0} + B'_{m,1}\theta' + B'_{m,2}\theta'^2 + \cdots\cdots, \end{aligned}\right\} \qquad \left.\begin{aligned} a_m &= a'_{m,0} + a'_{m1}\theta' + a'_{m,2}\theta'^2 + \cdots\cdots, \\ b_m &= b'_{m,0} + b'_{m,1}\theta' + b'_{m,2}\theta'^2 + \cdots\cdots, \\ c_m &= c'_{m,0} + c'_{m,1}\theta' + c'_{m,2}\theta'^2 + \cdots\cdots, \\ d_m &= d'_{m,0} + d'_{m,1}\theta' + d'_{m,2}\theta'^2 + \cdots\cdots. \end{aligned}\right\} \tag{15}$$

If we substitute (15) into the differential equation and equate the coefficient of θ^{-1}, the following condition will be given as $\theta \to 0$:

$$\left.\begin{aligned} A_{m,1} &= -a_{m,0}, \\ B_{m,1} &= -b_{m,0}. \end{aligned}\right\} \quad m = 1, 2 \tag{16}$$

3) around $\theta = \pi$

The conditions as (12), (13), and (14) are readily derived by putting $\theta' = \pi - \theta$.

The above conditions (12) and (13) are approximately satisfied by our total electric field which is obtained by extrapolating the magnetic potential at middle latitudes and using Maeda's conductivity [4]. In the calculation we assume that (12) and (13) are

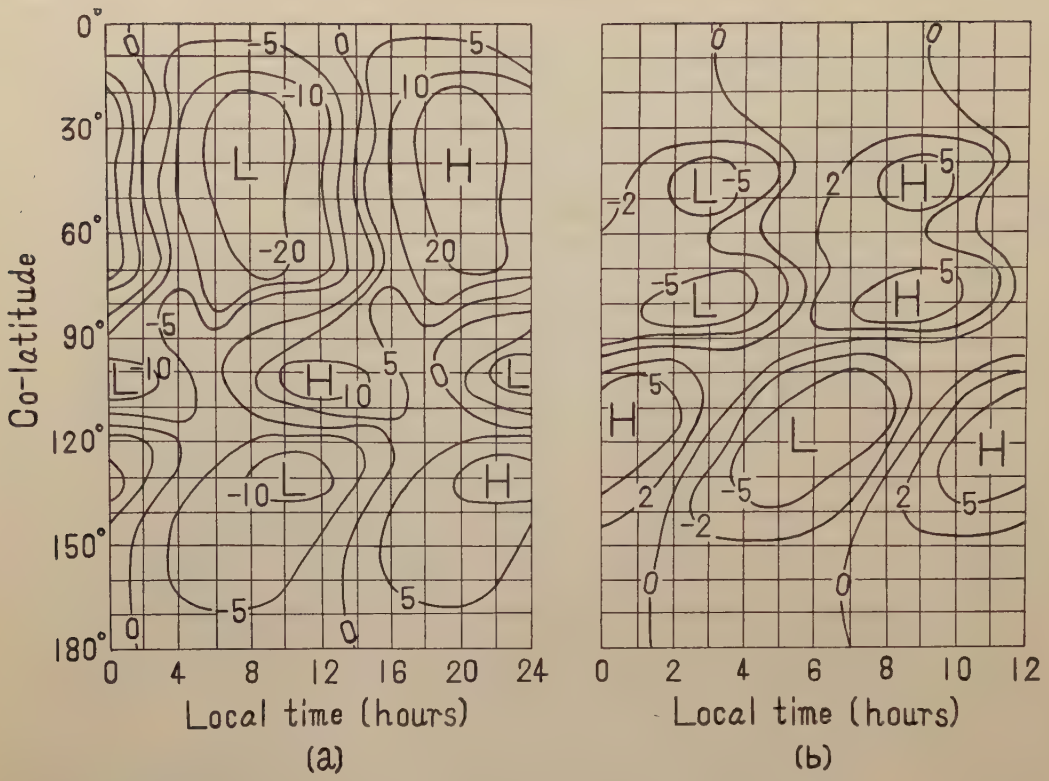

Fig. 3 Distribution of $\frac{1}{a\omega}\frac{p'}{\rho_0}$ which is proportional to the pressure variation
Unit : 10^2 *cm sec*$^{-1}$
(a) Diurnal component corresponding to Fig. 2 (a)
(b) Semi-diurnal component corresponding to Fig. 2 (b)

strictly satisfied. M. Hirono and T. Kitamura assumed that S_q current vanishes at the pole [5]. Their assumption seems to be mathematically rather restrictive as known from (12) and (13). We have obtained a particular integral by Runge-Kutta's method, starting from $\theta=0$ and π up to $\frac{\pi}{2}$.

The general solution of (7) and (8) consists of this particular integral and the complementary solution, viz.

$$S=S_1+CS_0,$$

where C is an integration constant, S_1 a particular integral and S_0 the complementary integral which is

$$S_0=\sin^m\theta F\left(\frac{m}{2},\ \frac{m}{2}|1+m|\sin^2\theta\right),$$

where F stands for the hypergeometric function. The boundary condition to be satisfied at the equator is that the induced field must vanish there and hence the static field determined by (7) and (8) is equal to the total electric field deduced from S_q variations. From E_y we can determine C.* A_m and B_m for $m=1$ are shown in Fig. 1.

* From E_x at $\theta=\frac{\pi}{2}$ it appears possible to determine C. However, $\frac{dS}{d\theta}$ is necessarily qual to E_x at $\theta=\frac{\pi}{2}$ as proved in 2), because the derivative of the complementary function S_0 vanishes at $\theta=\frac{\pi}{2}$.

4. Wind Systems

Substraction of the static field from the total field gives the induced field, from which the wind velocity are readily obtained by using (4) in section 2. The wind systems of the diurnal and the semi-diurnal components are shown in Fig. 2. Pressure variatons corresponding to these wind systems are shown in Fig. 3.

From these figures it is known that in summer the diurnal wind velocity is greater than the semi-diurnal, and in winter both diurnal and semi-diurnal wind velocities have almost the same magnitude. In Part I and II we obtained the wind systems in the mean solstice. The diurnal wind velocity was shown to be greater than the semi-diurnal. Therefore, actually, the mean solstice corresponds rather to summer.

If the wind velocities of both solstice seasons are compared, it is found that the diurnal wind velocity is greater in summer than in winter, whereas the semi-diurnal wind velocity is a little greater in winter than in summer. The diurnal velocity is 30～40 m/s in summer and 30～15 m/s in winter in middle latitudes. The semi-diurnal velocity is 20～30 m/s in winter and 10～15 m/s in summer in middle latitudes. As in Part II, the cyclonic character is noticeable in the diurnal component. The semi-diurnal pressure variation reaches the maximum value earlier in the morning in summer than in winter.

5 Discussions

In recent years the observation of the wind motion in the ionosphere has been made by using various techniques at some locations [6] [7] [8] [9]. However, consistent results have not been attained as yet, presumably because of difficulty in the analysis of the data.

Our calculation shows that in summer the diurnal wind velocity is greater than the semi-diurnal; the former being about 2 times greater than the latter in middle latitudes. Further it is shown that the diurnal wind velocity is greater in summer than in winter. These results seems to roughly agree with those obtained from the wind observation by L. Harang and K. Pedersen [9]. However, our results are discrepant with what we expect from observation of the daily pressure variation on the ground as well as with an observational result obtained by J. S. Greenhow and E. L. Neufeld in England [8]. Their results showed that no regular diurnal velocity had been detected.

The ionospheric conductivity used in our calculation is based on the assumption that the electron density at night is 1/12 of that at noon. If this value is unavailable, our calculation should be revised. Nocturnal ionization has recently been studied by A. P. Mitra on a semi-empirical basis [10]. His estimate seems to agree with that value.

There is a considerably rapid shift of the phase with height in the atmospheric oscillation at the bottom of E region. Hence, as suggested previously [1], our result obtained by taking mean with height may not represent the actual state. However, a simple calculation shows that any conspicious change will not come in our present result when the shift of the phase is taken into consideration [11].

It has been assumed that the wind motion in the ionosphere is altogether periodic. If non-periodic motion exists, our result will suffer some alterations.

At present the results of various wind observations seem somewhat imcompatible with each other. It is desirable that wind observation be conducted at many places. Further theoretical study is very important.

6. Acknowlegements

The author wishes to express his sincere gratitude to Prof. M. Hasegawa, Prof. K. Maeda and Prof. S. Miyamoto for their encouragement and guidance.

He is also indebted to Dr. M. Ota, Dr. T. Sakai, and Dr. M. Hirono for their helpful suggestions.

He is further grateful to Mr. Kijima who had the trouble to check the solution of the differential equation by Integro-Differential Analyser.

His heartfelt gratitude is due to Mr. R. H. Grant for careful reading the English typescript.

References

[1] S. Kato, J. Geomag. Geoelect., **8**, 24 (1956).
[2] M. V. Wilkes, Oscillation of the earth's atmosphere, Cambrige Univ. Press (1949).
G. I. Taylor, Proc. Roy. Soc., A **156**, 318 (1936).
C. L. Pekeris, Proc. Roy. Soc., A **171**, 434 (1939).
[3] H. Maeda, J. Geomag. Geoelect., **7**, 121 (1955)
[4] H. Maeda, J. Geomag. Geoelect., **9**, 86 (1957)
[5] M. Hirono and T. Kitamura, J. Geomag. Geoelect., **8**, 9 (1956).
[6] B. H. Brigge and M. Spencer, Rep. Prog. Phy., **17**, 245 (1954).
[7] J. A. Ratcliffe, Nature, **177**, 307 (1956).
[8] J. S. Greenhow and E. L. Neufeld, Phil. Mag., **1**, 1157 (1956).
[9] L. Harang and K. Pedersen, J. Geophys. Res., **62**, 183 (1957).
[10] A. P. Mitra, J. Atmosph. Terr. Phys., **10**, 153 (1957).
[11] H. Maeda, Private communication.

Corrections to the paper; Horizontal Wind Systems in the Ionosperic E region Deduced from the Dynamo Theory of the Geomagnetic S_q variation. Part II Rotating Earth
J. Geomag. Geoelect., VIII, 24 (1956)

There were some misprints in Appendix of the previons paper. In (Al. 5) the second term is $\frac{1}{\sin\theta\cos\theta}\frac{dA}{d\theta}$ instead of $\tan\theta\frac{dA}{d\theta}$. A is tramsformed as $A=z^{m/2}w$ instead of $A=z^2w$. In (A 2.5) the first and second expressions should be corrected as

$$v' = \frac{-1}{4a\omega^2}\frac{\sigma}{f^2-\cos^2\theta}\left\{\frac{\cos\theta}{f}\frac{d}{d\theta}+\frac{m}{\sin\theta}\right\}\Psi^{(m)}$$

$$= \frac{\sigma}{4a\omega^2}\frac{1}{\sin\theta}\frac{1}{f^2-\cos^2\theta}\left(\frac{\mu}{f}D-m\right)\Psi^{(m)}.$$

σ and $\frac{1}{f^2-\cos^2\theta}$ were missing in the paper.

Addendum

Before receiving the first galley proof the results of a systematic investigation of winds in the upper atmosphere had been reported (W. G. Elford, Mixed Commission on the Ionosphere, New York, August, 1957). According to that result the periodic components contain the diurnal as well as the semi-diurnal terms. Furthermore, the order of magnitude, the seasonal variation, and the sense of rotation, of the wind vectors are roughly agreeable with the result of our calculation.

LETTERS TO THE EDITORS

Distribution of Ions around charged Fine Wires

According to the results of the writer's measurement* of the dissipation of electricity from charged fine wires, the dissipation coefficients are given by

$$a=a_0\left(1+\frac{b}{r}\right), \tag{1}$$

where 'a' is the dissipation coefficient, a_0, b are constants, and r the radius of wire. On the basis of this relation some considerations on the distribution of ions around the charged fine wires were made.

When the wire is charged positive the negative ions would be collected around it due to the intense electric field, and the positive ions repelled away. The charges entered into the wire of unit length in time interval dt will be given by

$$dq'=2\pi r\rho kE\,dt, \tag{2}$$

where dq'=charges flowing into the wire,
ρ=density of charge at the surface of the wire,
E=intensity of the electric field,
k=mobility of ions.

Since,

$$rE=2q=2CV, \tag{3}$$

where q is the charge of the wire per unit length at any time, C is the capacity of it with respect to the earth and V is the potential, from (2) and (3)

$$dq'=4\pi k\rho q dt. \tag{4}$$

On the other side the charge on the wire dissipates dq in dt, then

$$-dq=dq'=4\pi k\rho q dt. \tag{5}$$

By the definition of the dissipation coefficient we get,

$$a=-\frac{1}{q}\frac{dq}{dt}=4\pi k\rho. \tag{6}$$

While the distribution of ρ around fine wires accompanied strong field have not been clarified at present, so we assume ρ is proportional to E and C, i.e.

$$\rho=\rho_0'+\mu' EC, \tag{7}$$

where ρ_0' is the value of ρ for weak field and μ' the constant. Now, the capacity of the

* Memoirs of The Faculty of Liberal Arts Fukui University Series II, Natural Science No. 6, Part 2 1956

wire is given by

$$C=\frac{1}{2\log_e 2h/r} \quad \text{for} \quad h \gg r, \tag{8}$$

where h is the distance between the wire and the earth. Within the limits of values of r (0.044~0.0063 cm), which were used in writer's measurements, C is briefly represented by the next approximate formula;

$$C=\alpha+\beta r, \tag{9}$$

where α and β are constants, whose values are 0.073 and 0.68 respectively. From (7) and (9) we obtain

$$\rho=\rho_0\left(1+\frac{\mu}{r}\right), \tag{10}$$

neglecting small quantities. Here ρ_0 and μ are as follows;

$$\rho_0=\rho_0'+4\mu'\alpha\beta V, \tag{11}$$

$$\mu=\frac{2\mu'\alpha^2 V}{\rho_0'+4\mu'\alpha\beta V}. \tag{12}$$

These constants should be determined in connection with the measurement. Combinning (6) and (10), writing $4\pi k\rho_0=a_0$, we get

$$\begin{aligned} a&=4\pi k\rho_0\left(1+\frac{\mu}{r}\right)\\ &=a_0\left(1+\frac{\mu}{r}\right) \end{aligned} \tag{13}$$

Taking $\mu=b$, equation (13) is identical with (1). The term $4\mu'\alpha\beta V$ in (11) is small compared with ρ_0', therefore (11) and (12) becomes

$$\left.\begin{aligned} \rho_0'&=\rho_0\\ \mu&=\frac{2\mu'\alpha^2 V}{\rho_0} \end{aligned}\right\} \tag{14}$$

approximately. In (14) it is clear that μ is not a constant in the strict sense, and it is a function of V. But by simple order estimation, it is possible to understand that the next relation holds;

$$\left|\frac{\partial\rho}{\partial r}\right| \gg \left|\frac{\partial\rho}{\partial V}\frac{dV}{dt}\right|. \tag{15}$$

Accordingly we may take ρ depends only on the radius of the wire in the calculation of 'a' by (6). In other word in a small time interval it may be permitted to take 'a' constant independent of time.

Let the number of ions around the wire be n, by (6), (10), (13),

$$\begin{aligned} n&=\frac{\rho}{e}=\frac{a}{4\pi ke}\\ &=\frac{a_0}{4\pi ke}\left(1+\frac{\mu}{r}\right), \end{aligned} \tag{16}$$

or

$$n=n_0\left(1+\frac{b}{r}\right), \quad (\mu=b). \tag{17}$$

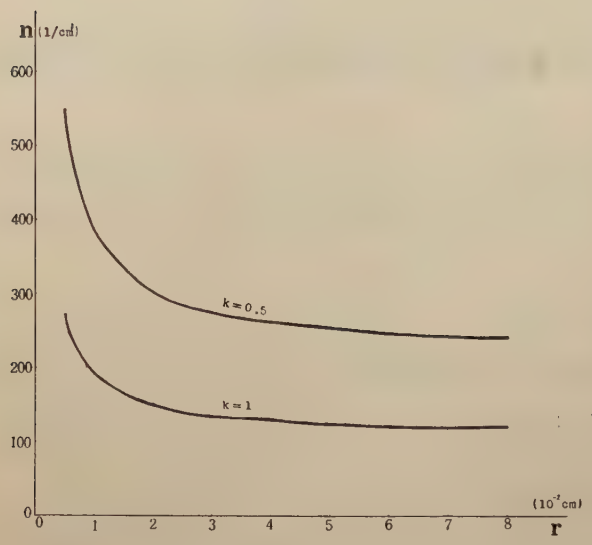

Fig. 1

where $n_0=a/4\pi ke$ and e is the elementary charge respectvely. By (17) computations of ion number around charged wires are possible. In Fig. 1, it is shown the ion number for $k=1$ and 0.5 (cm/sec/volt/cm), taking as the mean value $a_0=2.00\times10^{-4}$ (1/sec) ($\rho_0=2.00\times10^{-4}/4\pi k$) and $b=0.0074$ from the measurement. For large r, $b/r\to0$, therefore $n_0(=\rho_0/e)$ in (17) may be regarded to show the number of ions around the conductor of large r. On account of this the n_0 have been taken as the ion number in free atmosphere. And it is noteworthy that the values in Fig. 1 are the one obtained in the laboratory without air circulation.

The writer is indebted to Professor Y. Tamura of Kyoto University for his invaluable advice and encouragement.

Tôru SHIMIZU
Fukui Univesity

Wind Systems for the Geomagnetic S_d Field

Horizontal wind-systems in the ionospheric E-region required to produce the solar daily magnetic variation on disturbed days (say, S_d) are deduced along the same line as in the case of S_q [1, 2]. The data used are the horizontal intensity of the geomagnetic S_d-variations* at 62 stations over the world for the mean solstice during the International Polar Year, 1932–33. The harmonic coefficients of the North (ΔX) and East (ΔY) components are plotted in Fig. 1. The dotted (for ΔX) and full (for ΔY) lines show a smooth distribution of the coefficients, where the curves between 60°N and 60°S are derived from the potential of the S_q [3] and S_D [4] fields* for the mean solstice (see Table 1), and the curves in latitudes higher than 60° are deduced directly from the distribution of the coefficients.

The distribution of electrical conductivity on disturbed days is assumed as follows:

$$\begin{Bmatrix} \sum_{xx} \\ \sum_{yy} \\ \sum_{xy} \end{Bmatrix} = \begin{Bmatrix} \sum_{xx0}(\varphi) \\ \sum_{yy0}(\varphi) \\ \sum_{xy0}(\varphi) \end{Bmatrix} \Psi(\varphi, t),$$

where φ is the latitude, and t the local time. The values of $\sum_0$'s are given in Table III (Model B) of a

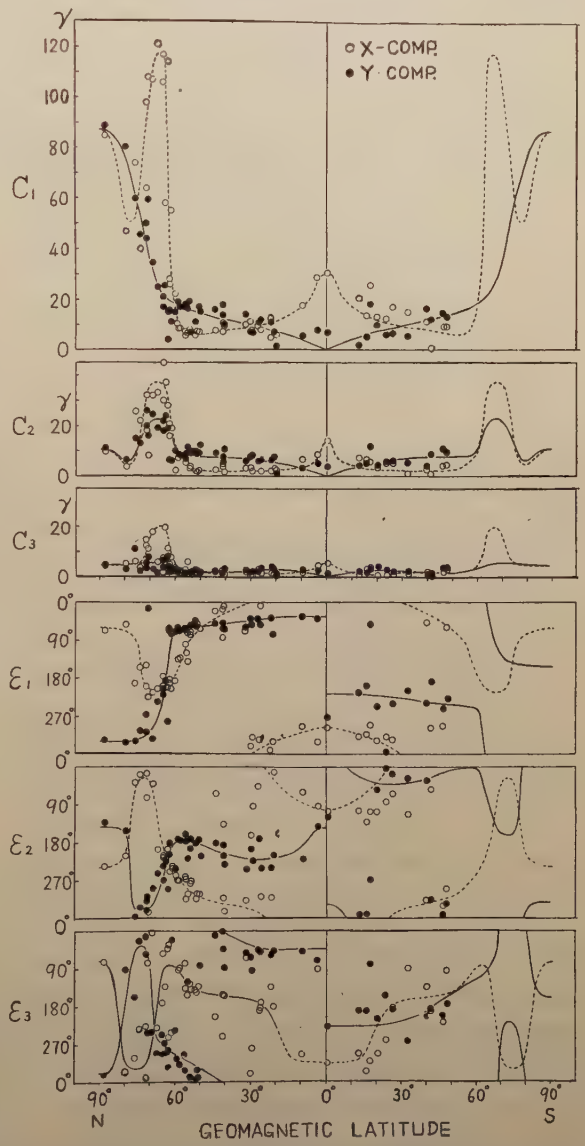

Fig. 1 Latitude-distributions of the harmonic coefficients for the geomagnetic North (ΔX) and East (ΔY) components of the geomagnetic S_d-variations for the mean solstice. The dotted (for ΔX) and full (for ΔY) lines show a smooth distribution of the coefficients.

* In this paper, the disturbance-daily variation S_D is defined as the average daily variation on five international disturbed minus quiet days (i. e., $S_d - S_q$), so that $S_d = S_q + S_D$, and S_D seems an average of the diurnally varying part D_s of magnetic storms.

Table 1. Spherical harmonic coefficients for the geomagnetic S_q- and S_D-fields analyzed in the form

$$V=r_0\sum_n\sum_m(a_n^m\cos mt+b_n^m\sin mt)P_n^m(\cos\theta),$$

using the Second Polar Year data. (Unit=γ)

	S_q			S_D	
m	n	a_n^m	b_n^m	n	a_n^m	b_n^m
1	2	8.40	−2.35	2	−0.71	−6.85
	4	−1.75	0.40	4	−0.23	−1.97
	6	0.21	0.12	6	0.53	−0.46
2	3	−4.15	1.69	3	2.32	−3.46
	5	0.14	−0.15	5	−0.94	0.38
	7	−0.02	0.22	7	0.06	−0.69
3	4	1.42	−0.86	4	−0.38	0.57
	6	0.30	−0.02	6	−0.19	0.53

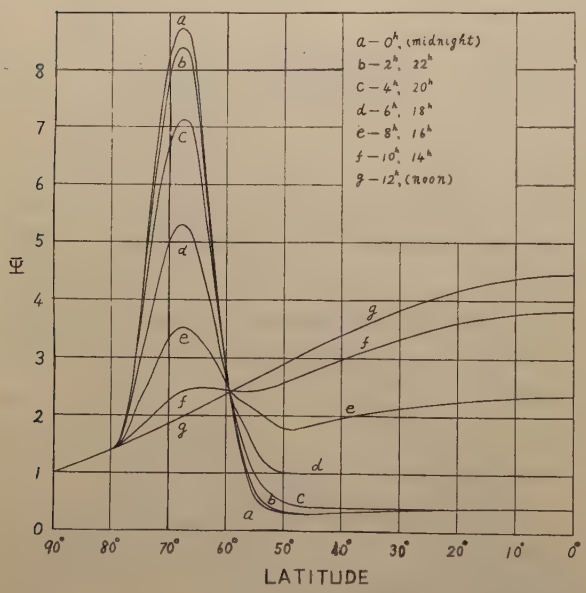

Fig. 2 Latitude-distributions of $\Psi(\varphi, t)$ at intervals of two-hours.

previous paper [5], and the latitude distributions of $\Psi(\varphi,t)$ at intervals of two hours are illustrated in Fig. 2 which is reasonably deduced from f_oE and f_oE_s of the ionosphere at sunspot-minimum.

The total electric field for S_d is calculated by using the geomagnetic intensity and the conductivity prepared above, and the dynamo equation is solved, consequently S_d wind-systems are obtained. Since the method of treatment is the same as that for the S_q-winds [2], its detailed descriptions are not repeated here. The distributions of wind-velocity thus obtained are shown in Fig. 3 for each of the diurnal and semi-diurnal components, and the winds for S_q [1] are also shown in Fig. 4 for comparison. It is seen from these figures that the wind-velocity for S_d in the polar regions is very great (about 200~400 m/s) as compared with that for S_q, and the wind-pattern is also different from that for S_q, especially in the auroral zone. From these results we may conclude that in order to interpret the diurnally varying part of magnetic storms by a dynamo theory, without assuming an exceptionally enhanced conductivity in the polar regions as made by Jacobs and Obayashi [6], strong polar wind-systems which are quite different from those for the S_q-field are required.

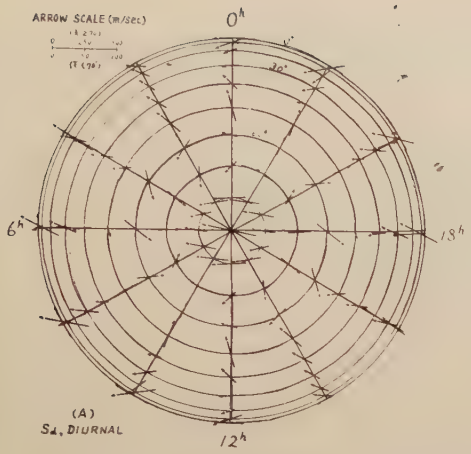

Fig. 3 Wind-systems for the S_d-field, viewed from above the North pole: (A) the diurnal and (B) the semi-diurnal component.

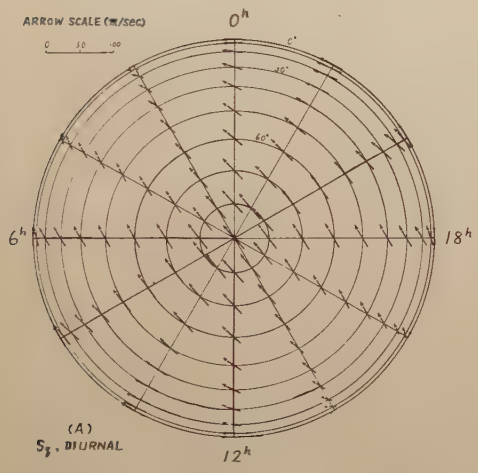

Fig. 4 Wind-systems for the S_q-field, viewed from above the North pole: (A) the diurnal and (B) the semi-diurnal component.

References

[1] H. Maeda, J. Geomag. Geoelectr., **7,** 121 (1955).
[2] H. Maeda, J. Geomag. Geoelectr., **9,** 86 (1957).
[3] H. Maeda, J. Geomag. Geoelectr., **5,** 39 (1953).
[4] T. Namikawa, (to be published).
[5] H. Maeda, Rep. Ionosph. Res. Japan, **10,** 49 (1956).
[6] J. A. Jacobs and T. Obayashi, A dynamo theory of magnetic storms, Contract AF 19 (604)-761, Sci. Rep. No. 4, March (1957).

Hiroshi MAEDA

Department of Earth Science,
Yoshida College, Kyoto University

Meeting of the Society of Terrestrial Magnetism and Electricity:

The 22nd General Meeting was held at the Kakioka Magnetic Observatory on October 9–11, 1957.

Number of the Reports read at the Meeting:

Geomagnetism, 16; Ionosphere, 6; Night Airglow, 4; Cosmic Rays, 11; Rock Magnetism, 5; Earth Current, 2; Atmospherics, 3; Atmospheric Electricity and Radio Meteorology, 7.

昭和32年11月25日　印刷
昭和32年12月1日　發行
第9卷　第2號

編輯兼發行者　日本地球電氣磁氣學會
代表者　長谷川万吉

印刷者　京都市南区上鳥羽唐戸町63
田中幾治郎

賣捌所　丸善株式會社京都支店
丸善株式會社 東京・大阪・名古屋・仙台・福岡

JOURNAL OF GEOMAGNETISM AND GEOELECTRICITY

Vol. IX No. 2

1957

CONTENTS

Thermo-Remanent Magnetism and Coercive Force of the Ilmenite-Hematite Series ..... S. UYEDA 61

Solar Activity and Cosmic Radiation ..... R. R. BROWN 79

Horizontal Wind Systems in the Ionospheric E Region Deduced from the Dynamo Theory of the Geomagnetic S_q Variation. Part III.....H. MAEDA 86

Disturbances in the Ionospheric $F2$ Region Associated with Geomagnetic Storms III. Auroral Latitudes..... T. SATO 94

Horizontal Wind Systems in the Ionospheric E Region Deduced from the Dynamo Theory of the Geomagnetic S_q Variation. Part IV..... S. KATO 107

LETTERS TO THE EDITORS:

Distribution of Ions around Charged Fine Wires.....T. SHIMIZU 116

Wind Systems for the Geomagnetic S_d Field..... H. MAEDA 119

electricity is controlled by the ionization equilibrium process, we will discuss the local anomaly of the diurnal variation of the atmospheric electric field of the basis of the fundamental equation.

2. The diurnal variation of the atmospheric electric field, conductivity and space charge at Hongo

A few examples of the record of the atmospheric electric field are shown in Fig. 1. The mean hourly values of the electric field in each month are shown in

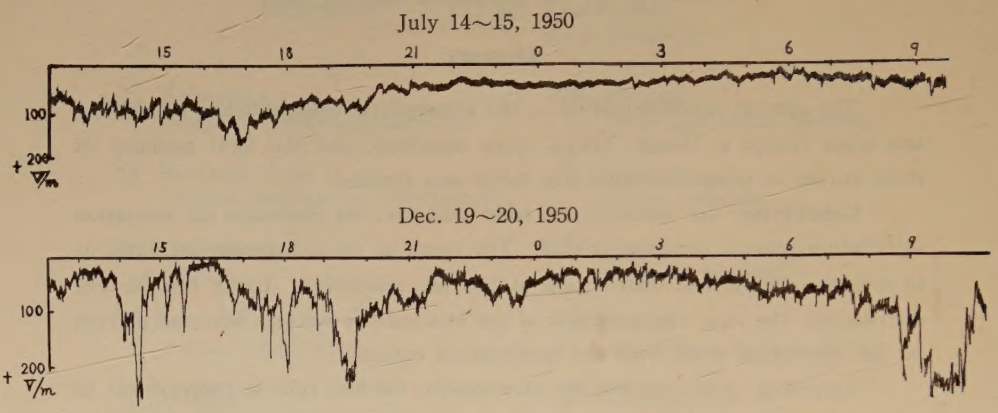

Fig. 1 The examples of th observed record of the atmospheric electric field at Hongo.

Table 1. In Fig. 2-4 are shown the mean diurnal variation curves of the electric field, space charge and conductivity in summer and winter. Uses are made of the record covering the period from Aug. 1949 to Feb. 1952. The seasonal change can be readily seen in the figures. Another interesting thing is that in winter, the conductivity is in general low and the electric field is high, but as the year progresses into the summer the conductivity increases while the electric field decreases. The most interesting feature is the remarkable difference between diurnal variation in summer and winter. In winter season the variation is generally regular in character, and the maximum value of the electric field occurs at about 10 h L.M.T.. In summer season the diurnal

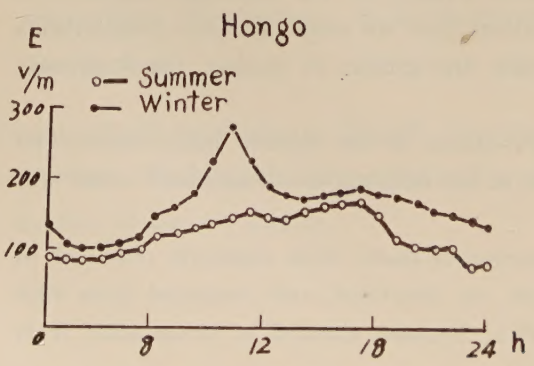

Fig. 2 The diurnal variation curves of the electric field at Hongo.

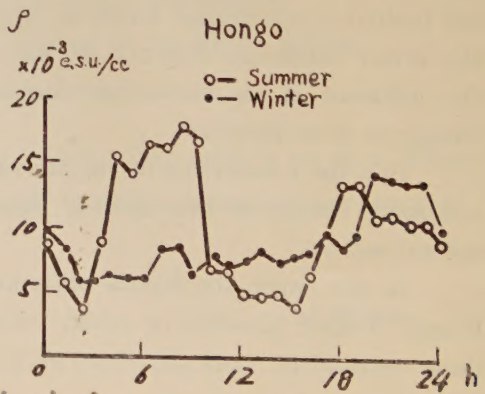

Fig. 3 The diurnal variation curves of the space charge at Hongo.

The General Expression of the Diurnal Variation of the Atmospheric Electric Field Considering the Influence of the Eddy Diffusion near the Ground.

By Minoru KAWANO

Electrotechnical Laboratory, Tokyo, Japan

(Read Oct. 11, 1957; Received Nov. 10, 1957)

Abstract

The diurnal variation curves of the atmospheric electric field, conductivity and space charge at Hongo, Tokyo, were described, and the local anomaly of these curves in urban condition was fairly well clarified.

Considering the influence of eddy diffusion, we discussed the ionization equilibrium process near the ground. The result of the calculation permitted us to estimate the vertical distribution of the air resistivity. Using the vertical distribution, the local characteristic of the atmospheric electric field was derived on the theoretical basis from the fundamental equation.

According to the results, the atmospheric electric field is proportional to the space charge and the square root of the coefficient of eddy diffusivity. This consideration shows that the diurnal variation of the atmospheric electric field can be explained by the fundamental equation of the electro-magnetic field assuming the Ohm's law.

1. Introduction

The several authors [1], [2], [3] have made comparisons of diurnal variations of the atmospheric electric field observed at many stations on land in the world. Mühleisen [4] has carried out the simultaneous observations at two stations, which are situated in comparatively short distance in the different condition each other, and concluded that the complicated variation in the urban condition seems to be caused by the positive space charge which is originated densely by the industrial activities in the urban condition. Kawano [5] has clarified that we must take into consideration the influence of the convection current near the ground to explain the stationary change in short duration.

But, the comparison of the diurnal variations of the electric field, conductivity and space charge at two stations situated in the different conditions each other was not carried out.

In this paper, the diurnal variation curves of these three elements obtained at Hongo, Tokyo, situated in urban condition are described, and compared them with those obtained by Aoki and others [6], [7], [8] at Tanashi, situated at 25 km apart from Hongo.

Considering that the stationary change in each element of the atmospheric

JOURNAL OF GEOMAGNETISM AND GEOELECTRICITY

The fields of interest of this quarterly Journal are as follows:

Terrestrial Magnetism	Aurora and Night Airglow
Atmospheric Electricity	The Ozone Layer
The Ionosphere	Physical States of the Upper Atmosphere
Radio Wave Propagation	Solar Phenomena relating to the Above Subjects
Cosmic Rays	Electricity within the Earth

The text should be written in English, German or French. The price is set as 1 dollar per number. We hope to exchange this Journal with periodical publications of any kind in the field of natural science.

The Editors

JOURNAL
OF
GEOMAGNETISM
AND
GEOELECTRICITY

VOL. IX NO. 3

SOCIETY
OF
TERRESTRIAL MAGNETISM AND ELECTRICITY
OF
JAPAN

1957
KYOTO